

Models of circumstellar molecular radio line emission*

Mass loss rates for a sample of bright carbon stars

F. L. Schöier¹ and H. Olofsson¹

Stockholm Observatory, SE-133 36 Saltsjöbaden, Sweden

A&A in press

Abstract. Using a detailed radiative transfer analysis, combined with an energy balance equation for the gas, we have performed extensive modelling of circumstellar CO radio line emission from a large sample of optically bright carbon stars, originally observed by Olofsson et al. (ApJS, 87, 267). Some new observational results are presented here. We determine some of the basic parameters that characterize circumstellar envelopes (CSEs), e.g., the stellar mass loss rate, the gas expansion velocity, and the kinetic temperature structure of the gas. Assuming a spherically symmetric CSE with a smooth gas density distribution, created by a continuous mass loss, which expands with a constant velocity we are able to model reasonably well 61 of our 69 sample stars. The derived mass loss rates depend crucially on the assumptions in the circumstellar model, of which some can be constrained if enough observational data exist. Therefore, a reliable mass loss rate determination for an individual star requires, in addition to a detailed radiative transfer analysis, good observational constraints in the form of multi-line observations and radial brightness distributions. In our analysis we use the results of a model for the photodissociation of circumstellar CO by Mamon et al. (1988). This leads to model fits to observed radial brightness profiles that are, in general, very good, but there are also a few cases with clear deviations, which suggest departures from a simple r^{-2} density law.

The derived mass loss rates span almost four orders of magnitude, from $\sim 5 \times 10^{-9} M_{\odot} \text{ yr}^{-1}$ up to $\sim 2 \times 10^{-5} M_{\odot} \text{ yr}^{-1}$, with the median mass loss rate being $2.8 \times 10^{-7} M_{\odot} \text{ yr}^{-1}$. We estimate that the mass loss rates are typically accurate to $\sim 50\%$ within the adopted circumstellar model. The physical conditions prevailing in the CSEs vary considerably over such a large range of mass loss rates. Among other things, it appears that the dust-to-gas mass ratio and/or the dust properties change with the mass loss rate. We find that the mass loss rate and the gas expansion velocity are well correlated, and that both of them clearly depend on the pulsational period and (with larger scat-

ter) the stellar luminosity. Moreover, the mass loss rate correlates weakly with the stellar effective temperature, in the sense that the cooler stars tend to have higher mass loss rates, but there seems to be no correlation with the stellar C/O-ratio. We conclude that the mass loss rate increases with increased regular pulsation and/or luminosity, and that the expansion velocity increases as an effect of increasing mass loss rate (for low mass loss rates) and luminosity.

Five, of the remaining eight, sample stars have detached CSEs in the form of geometrically thin CO shells. The present mass loss rates and shell masses of these sources are estimated. Finally, in three cases we encounter problems using our model. For two of these sources there are indications of significant departures from overall spherical symmetry of the CSEs.

Carbon stars on the AGB are probably important in returning processed gas to the ISM. We estimate that carbon stars of the type considered here annually return $\sim 0.05 M_{\odot}$ of gas to the Galaxy, but more extreme carbon stars may contribute an order of magnitude more. However, as for the total carbon budget of the Galaxy, carbon stars appear to be of only minor importance.

Key words: Stars: AGB and post-AGB – Stars: carbon – circumstellar matter – Stars: late-type – Radio lines: stars

1. Introduction

The carbon star phenomenon, i.e., the presence of stars for which the abundance of carbon exceeds that of oxygen in the atmospheres, occurs during the final evolutionary stage of low to intermediate mass stars ($\sim 1-10 M_{\odot}$; Wallerstein & Knapp 1998), and it is believed to be due to a dredge-up process driven by quasi-periodic He-shell flashes (Straniero et al. 1997). These stars, located on the asymptotic giant branch (AGB), lose copious amounts of matter ($\sim 10^{-8}-10^{-4} M_{\odot} \text{ yr}^{-1}$) in an intense stellar wind. In fact, it is the mass loss that determines the AGB lifetime and not the nuclear burning processes. Hence, a determination of the mass loss characteristics, i.e., the dependence on time, mass, chemistry, metallicity, etc., is of utmost importance for our understanding of late stellar evolution.

Send offprint requests to: F. L. Schöier (fredrik@strw.leidenuniv.nl)

* Presented in this paper is observational data collected using the Swedish-ESO submillimetre telescope, La Silla, Chile, the 20 m telescope at Onsala Space Observatory, Chalmers Tekniska Högskola, Sweden, and the NRAO 12 m telescope located at Kitt Peak, USA.

The mass loss creates a circumstellar envelope (CSE) of gas and dust around the star. The low temperature of the central star allows the formation of a wide variety of molecular species in its atmosphere, and the expanding gas is therefore mainly in molecular form. The chemistry in the CSE itself can be very rich, and it depends on the C/O-ratio, the thickness of the envelope, and the strength of the ambient ultraviolet radiation field. Presently, ~ 60 different molecular species have been identified in CSEs around AGB-stars (Olofsson 1997).

The study of AGB-CSEs is important for the understanding of the late stages of stellar evolution as mentioned above. In addition, an understanding of the atmospheric and circumstellar chemistry is required to determine the elemental abundances in these winds, which contribute to the chemical evolution of the interstellar medium (Busso et al. 1999). Finally, since AGB stars are the progenitors of planetary nebulae (PNe), the CSEs are very likely important ingredients in the formation of PNe (Kwok 1993).

Observations of molecular millimetre-wave line emission have proven to be one of the best tools for studying the structure, kinematics, and chemistry of the CSEs, and CO and OH observations have proven particularly useful for the determination of accurate mass loss rates [see Olofsson (1996) and references therein].

While the overall picture of mass loss on the AGB is fairly well understood, some of the underlying physical principles are not. The prevailing theory, which needs to be thoroughly tested observationally, is that the mass loss occurs in a two stage process. First the pulsations of the star deposit energy in the atmosphere, leading to a considerably increased scale height, and sufficient matter at low enough temperatures for efficient dust formation. Radiation pressure on the dust grains accelerate the dust wind to its terminal expansion velocity in the second stage. The gas is momentum coupled, through collisions, to the dust, and it will be effectively dragged along. The mechanisms that cause the mass loss to vary on a wide range of time scales still need to be pinpointed. Eventually, the possibility of mass ejected in clumps has to be addressed, although in this paper we will consider only a smooth spherically symmetric wind.

This study of an essentially complete sample of visually bright, relatively unobscured carbon stars will hopefully increase our knowledge of the modelling of circumstellar molecular radio line emission, the mass loss characteristics, the circumstellar chemistry, the elemental abundances in the winds, and possibly the evolutionary status of these objects. It will also provide us with the tools required to determine the properties of higher mass loss rate objects, for which the central star may be completely obscured.

In this paper the basic physical characteristics of the CSEs, e.g., the stellar mass loss rate, the gas kinetic temperature, and the gas expansion velocity, are determined using a radiative transfer analysis of the observed ^{12}CO (hereafter CO) millimetre-wave line emission. The CO molecule is particularly well suited for this purpose, since it is difficult to photodissociate and easy to excite through collisions, and thus is a very good tracer of the molecular gas density and temperature.

Table 1. Data on telescopes and receivers used.

Tel.	Trans.	ν [GHz]	$T_{\text{rec}}(\text{SSB})$ [K]	θ_{mb} [""]	η_{mb}	η_{m}^*
OSO	CO(1–0)	115.271	100	33	0.5	
	CO(1–0)	115.271	110	45	0.7	
	CO(2–1)	230.538	110	23	0.5	
	CO(3–2)	345.796	300	16	0.25	
NRAO	CO(1–0)	115.271	80	55	0.55	0.84
	CO(2–1)	230.538	200	27	0.30	0.45

Furthermore, the molecular excitation is of a quasi-thermal nature which simplifies detailed modelling.

2. Observations

2.1. The sample

We have selected a sample of 68 bright N- and J-type carbon stars for which circumstellar CO emission was detected by Olofsson et al. (1993a). Their original sample consisted of carbon stars brighter than $K=2$ mag., in total 120 sources. The detection rate for all the carbon stars searched for circumstellar CO was as high as 72%. The original sample is thought to be close to complete to distances below 1 kpc [it is estimated that about a third of the carbon stars within this distance are missing, presumably the ones with thick and dusty CSEs, i.e., the high mass loss objects (Olofsson et al. 1993a)], and for distances below 500 pc all sources (a total of 41) were detected in CO (note that the distances used in this paper are generally lower than those adopted in Olofsson et al. 1993a). These facts taken together led to the conclusion that the great majority of all N-type carbon stars are losing mass at a rate higher than about $10^{-8} M_{\odot} \text{ yr}^{-1}$. They do not, however, constitute a homogeneous group in terms of circumstellar properties. Instead they show a wide range of gas expansion velocities and mass loss rates, presumably due to differences in mass, evolutionary stage, etc.. In addition, the reasonably well studied, high mass loss rate carbon star, LP And (also known as IRC+40540), is included in our analysis, since it provides a good test case for the radiative transfer model.

The CO ($J=1 \rightarrow 0$ and $J=2 \rightarrow 1$) observations presented in Olofsson et al. (1993a) were obtained using the 20 m telescope at Onsala Space Observatory (OSO), Sweden, the 15 m Swedish-ESO sub-millimetre telescope (SEST) at La Silla, Chile, and the IRAM 30 m telescope at Pico Veleta, Spain, during the years 1986–1992.

2.2. New observations

We have supplemented the original data with new CO observations of some of the sample stars. In particular, in the $J=3 \rightarrow 2$ line using the SEST (August 1992). Also some $J=1 \rightarrow 0$ and $J=2 \rightarrow 1$ data were obtained at SEST (October 1998). A few sources were observed in the $J=1 \rightarrow 0$ and $J=2 \rightarrow 1$ lines with

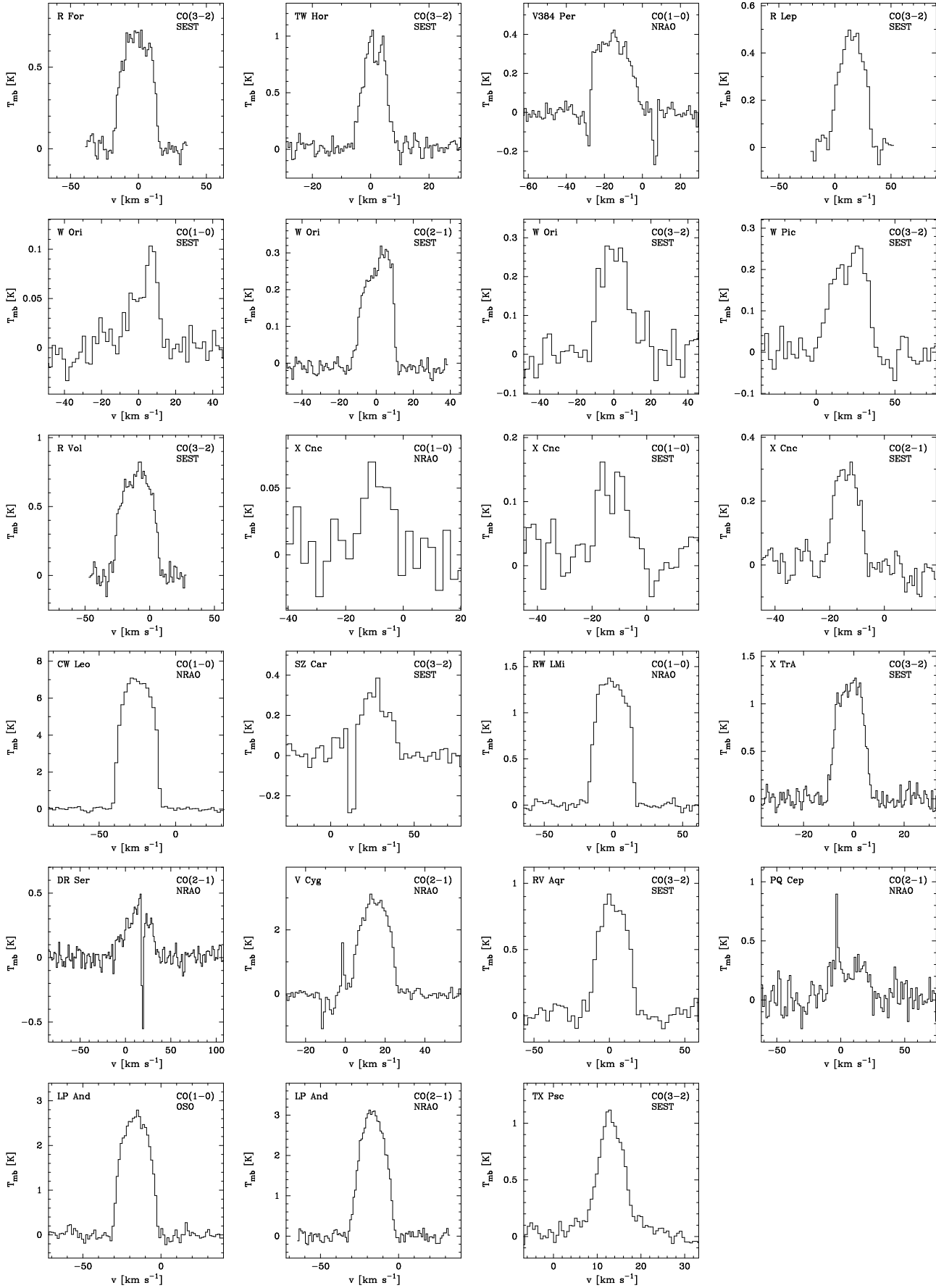


Fig. 1. New observations of circumstellar ^{12}CO line emission. The line observed and the telescope used are shown in the upper right corner of each panel.

Table 2. Observational results (see text for details). The intensity scale is thought to be accurate to within $\sim 20\%$.

Source	Tel.	Trans.	T_{mb} [K]	I_{mb} [K km s $^{-1}$]	v_{*} [km s $^{-1}$]	v_{e} [km s $^{-1}$]	β
R For	SEST	3–2	0.70	17.9	−1.8	16.1	1.0
TW Hor	SEST	3–2	0.94	8.7	1.0	7.5	2.5
V384 Per ¹	NRAO	1–0	0.37	7.8	−16.4	11.5	0.5
R Lep	SEST	3–2	0.48	12.9	12.4	19.5	1.7
W Ori ¹	SEST	1–0	0.06	1.2	1.6	8.6	−0.7
	SEST	2–1	0.27	4.9	0.0	10.0	0.4
	SEST	3–2	0.27	4.8	−1.4	11.8	1.1
W Pic	SEST	3–2	0.24	6.3	20.7	13.9	0.4
R Vol	SEST	3–2	0.74	20.8	−10.6	16.9	0.8
X Cnc	NRAO	1–0	0.06	0.7	−10.3	7.6	1.3
	SEST	1–0	0.12	1.7	−12.8	8.6	1.0
	SEST	2–1	0.30	3.2	−14.3	7.5	1.7
CW Leo	NRAO	1–0	7.1	170.8	−25.9	14.3	0.7
SZ Car ¹	SEST	3–2	0.30	5.5	25.7	13.1	1.2
RW LMi	NRAO	1–0	1.3	36.4	−1.6	15.8	0.7
X TrA	SEST	3–2	1.2	15.3	−2.0	8.7	1.6
DR Ser ¹	NRAO	2–1	0.26	11.3	11.6	24.1	1.1
V Cyg	NRAO	2–1	2.9	50.1	14.2	11.0	1.1
RV Aqr	SEST	3–2	0.83	18.6	1.2	14.5	1.1
PQ Cep ¹	NRAO	2–1	0.28	8.7	6.3	24.1	0.0
LP And	OSO	1–0	2.6	57.0	−16.9	13.8	1.1
	NRAO	2–1	3.1	60.7	−17.1	14.0	1.7
TX Psc ²	SEST	3–2	1.0	7.0	1.0	7.5	2.0

¹Contamination by interstellar lines. ² β was fixed.

the NRAO 12 m telescope at Kitt Peak, USA (June 1998), and some $J=1\rightarrow 0$ data were obtained using OSO (1998 to 1999).

A summary of telescope and receiver data [the receiver temperature T_{rec} in single sideband mode (SSB), the full half power main beam width θ_{mb} , the main beam efficiency η_{mb} , and the corrected main beam efficiency η_{m}^*] at the observational frequencies are given in Table 1.

At SEST, a dual channel SIS mixer receiver was used to simultaneously observe at 115 GHz (the $J=1\rightarrow 0$ line) and 230 GHz (the $J=2\rightarrow 1$ line). At 345 GHz (the $J=3\rightarrow 2$ line), a single polarization SiS mixer receiver was used. As backends, two acousto-optical spectrometers (AOS) were used; one high resolution spectrometer (HRS) and one low resolution spectrometer (LRS). The wideband (1 GHz) LRS had 1440 channels separated by 0.7 MHz, whereas the narrow band (84 MHz) HRS used 2000 channels separated by 42 kHz.

For the NRAO 12 m observations we used a dual polarization SIS receiver. As backends two filterbanks, each with 256 channels and a channel separation of 1 MHz, were used. The spectra obtained at each of the polarizations were added to increase the signal-to-noise ratio. In addition, for strong sources, a millimetre autocorrelator (MAC) was used in order to obtain a higher velocity resolution. The MAC was used in a configuration where the usable bandwidth was 300 MHz and the resolution was 98 kHz.

At OSO, a single polarization SIS receiver was used for the observations. As backends two filterbanks, with bandwidths

of 512 MHz (MUL A) and 64 MHz (MUL B), were used. The MUL A used 512 channels separated by 1 MHz, and the MUL B filterbank used 256 channels with a separation of 250 kHz.

The SEST and OSO observations were made in a dual beamswitch mode, where the source is alternately placed in the signal and the reference beam, using a beam throw of about 12' at SEST and 11' at OSO. This method produces very flat baselines. The intensity scales are given in main beam brightness temperature, T_{mb} . $T_{\text{mb}}=T_{\text{A}}^*/\eta_{\text{mb}}$, where T_{A}^* is the antenna temperature corrected for atmospheric attenuation using the chopper wheel method, and η_{mb} is the main beam efficiency, see Table 1.

At the NRAO 12 m telescope the observations were carried out using a position switching mode, with the reference position located +10' in azimuth. This is the preferred observation mode for spectral line observations at the 12 m telescope. The raw spectra, which are stored in the T_{R}^* scale, were converted using $T_{\text{mb}}=T_{\text{R}}^*/\eta_{\text{m}}^*$, where η_{m}^* is the corrected main beam efficiency given in Table 1. The T_{R}^* scale is related to T_{A}^* through $T_{\text{R}}^*=T_{\text{A}}^*/\eta_{\text{fss}}$, where η_{fss} is the forward scattering and spillover efficiency.

Regular pointing checks were made on strong SiO masers (OSO, SEST) and strong continuum sources (NRAO). The pointing was usually consistent within $\sim 3''$ for SEST and OSO and $\sim 5''$ at NRAO. The uncertainties in the absolute intensity scales at the various telescopes are estimated to be about

$\pm 15-20\%$. However, due to the low efficiency of the SEST at 345 GHz, and the narrow beam, we consider these data to be particularly uncertain in terms of calibration.

The new observational results are summarized in Table 2 and the spectra are shown in Fig. 1. The line parameters, i.e., the main beam brightness temperature at the line centre (T_{mb}), the line centre velocity (v_*), and half the full line width (v_e), are obtained by fitting the following line profile to the data (Olofsson et al. 1993a)

$$T(v) = T_{\text{mb}} \left[1 - \left(\frac{v - v_*}{v_e} \right)^2 \right]^{\beta/2}, \quad (1)$$

where β is a parameter describing the shape of the line ($\beta=2$ represents a parabolic line shape, and $\beta < 0$ means a profile with horns at the extreme velocities). The integrated intensity (I_{mb}) is obtained by integrating the emission between $v_* \pm v_e$.

In addition, we have obtained publicly available data from the James Clerk Maxwell Telescope (JCMT) at Mauna Kea, Hawaii. The JCMT data are taken at face value. However, in the cases where there are more than one observation available, the derived line intensities are generally consistent within $\pm 20\%$. The good agreement with corresponding SEST intensities further support the reliability of the JCMT public data. Furthermore, interferometer observations of the CO($J=1 \rightarrow 0$) brightness distribution around some of our carbon stars have been obtained by Neri et al. (1998) using the IRAM Plateau de Bure interferometer (PdBI). The data are publicly available and have been used in this paper.

3. Radiative transfer

3.1. The Monte Carlo method

In order to model the circumstellar molecular line emission and to derive the basic characteristics of the CSEs we have developed a non-LTE radiative transfer code based on the Monte Carlo method [Bernes (1979); see also Schöier (2000), for details]. An accurate treatment of the molecular excitation is needed for a correct description of the radiative transfer in an expanding circumstellar envelope, e.g., the Sobolev approximation has been shown to introduce significant errors in these circumstances (e.g., Schönberg 1985). The Monte Carlo method is well suited for the study of CSEs, since it is very flexible and close to the physics and yet simple in principle. For instance, one may include very complex geometries and velocity fields without being forced away from the physics of the problem. Crosas & Menten 1997 have recently used the Monte Carlo method to model the circumstellar CO radio line emission of the prominent carbon star IRC+10216 (from hereon called CW Leo).

The aim of the radiative transfer is to obtain the steady-state level populations, of the molecule under study, using the statistical equilibrium equations (SE). In the Monte Carlo method information on the radiation field is obtained by simulating the line photons using a number of model photons, each representing a large number of real photons from all transitions consid-

ered. These model photons, emitted both locally in the gas as well as injected from the boundaries of the CSE, are followed through the CSE and the number of absorptions are calculated and stored. Photons are spontaneously emitted in the gas with complete angular and frequency redistribution (CRD), i.e., the local emission is assumed to be isotropic and the scattering are assumed to be incoherent. The weight of a model photon is continuously modified, to take the absorptions and stimulated emissions into account, as it travels through the CSE. When all model photons are absorbed in, or have escaped, the CSE the SE are solved and the whole process is then repeated until some criterion for convergence is fulfilled. Once the molecular excitation, i.e., the level populations, is obtained the radiative transfer equation can be solved exactly.

The main drawback of the Monte Carlo method is its slow convergence ($\sim \sqrt{N_{\text{iter}}}$). This is, however, usually outweighed by its great adaptability. One of our motivations for choosing the Monte Carlo method was to be able to treat varying mass loss rates, departures from spherical symmetry, and the possibility of a highly clumped medium. These complicating issues will be investigated in a future version of our Monte Carlo code.

3.2. The standard model

The numerical modelling of line emission from CSEs, where intricate interplays between physical and chemical processes take place, is a challenge. This applies, in particular, to the important inner regions of the CSE model, where very few observational constraints are available and our knowledge is very limited. In this analysis, we will neglect many of these complexities and assume a relatively simple, yet reasonably realistic, CSE model. By applying the model to a large sample we will derive fairly reliable mass loss rates, and we will also be able to pick out objects for which there appears to be clear deviations from the simple picture.

In what will be referred to as "the standard model" we assume a spherically symmetric CSE that expands at a constant velocity. In our data we see no evidence for gas acceleration in the CO emitting region. The CSE is divided into a number of discrete shells, each with its own set of physical parameters describing the state of the molecular gas. The density structure (as a function of distance, r , from the central star) can then be derived from the conservation of mass

$$\rho_{\text{H}_2} = n_{\text{H}_2} m_{\text{H}_2} = \frac{\dot{M}}{4\pi r^2 v_e}, \quad (2)$$

where \dot{M} is the hydrogen gas mass loss rate, and v_e is the gas expansion velocity taken from the line profile fits of Olofsson et al. (1993a) or Table 2. We assume that in the CSEs of interest here the hydrogen is in molecular form in the region probed by the CO emission (Glassgold & Huggins, 1983). The turbulent velocity is assumed to be equal to 0.5 km s^{-1} throughout the entire CSE.

The excitation of the CO molecules were calculated taking into account 30 rotational levels in each of the ground and

first vibrational states. The radiative transition probabilities and energy levels are taken from Chandra et al. (1996), and the rotational collisional rate coefficients (CO-H₂) are based on the results in Flower & Launay (1985). These are further extrapolated for $J > 11$ and for temperatures higher than 250 K. Collisional transitions between vibrational levels are not important due to the low densities and their short radiative lifetimes.

The kinetic gas temperature is calculated after each iteration in a self-consistent way, using the derived level populations, by solving the energy balance equation (e.g., Goldreich & Scoville 1976),

$$\frac{dT}{dr} = (2 - 2\gamma) \frac{T}{r} + \frac{\gamma - 1}{n_{H_2} k v_e} (H - C), \quad (3)$$

where γ is the adiabatic index [assumed to be equal to 5/3, but the results are not very sensitive to its exact value, see also Groenewegen (1994) and Ryde et al. (1999)], k is the Boltzmann constant, H is the total heating rate per unit volume, and C is the total cooling rate per unit volume. The first term on the right hand side is the cooling due to the adiabatic expansion of the gas. Additional cooling is provided by molecular line emission from CO and H₂. The molecular cooling due to CO is calculated from the derived level populations using the expression of Crosas & Menten (1997). For the H₂ cooling we use the approach by Groenewegen (1994). HCN could be an important coolant in the inner parts of the envelope (Cernicharo et al. 1996), but Groenewegen (1994) demonstrates that HCN cooling is only of minor importance. In the present version of the code HCN cooling is therefore not included (in a forthcoming paper, Schöier & Olofsson in prep., this issue will be addressed).

The mechanism responsible for the observed mass loss is probably (at least for the stars of interest here) radiation pressure acting on small dust grains, which in turn are coupled to the gas (e.g., Höfner 1999). The radiation pressure on the dust grains will give them a drift velocity, v_{dr} , relative to the gas (Gilman 1972; Goldreich & Scoville 1976; Kwan & Hill 1977)

$$v_{dr} = \left(\frac{L v_e Q}{M c} \right)^{1/2}, \quad (4)$$

where L is the luminosity, Q is the averaged momentum transfer efficiency, and c is the speed of light [see Sahai (1990) for a more elaborate treatment]. As a result of the dust-gas drift, kinetic energy of the order of $\frac{1}{2} m_{H_2} v_{dr}^2$ will be transferred to the gas each time a particle collides with a dust grain. This is assumed to provide the dominating heating of the gas (Goldreich & Scoville 1976; Kwan & Hill 1977),

$$H_{dg} = (n_d \sigma_d v_{dr}) \frac{1}{2} \rho_{H_2} v_{dr}^2, \quad (5)$$

where n_d is the number density of dust grains, and σ_d the geometrical cross section of a dust grain. Introducing the dust-to-gas mass ratio Ψ this equation can be written

$$H_{dg} = \frac{3}{8} m_{H_2}^2 n_{H_2}^2 \frac{\Psi}{a_d \rho_d} \frac{v_{dr}^3}{1 + \frac{v_{dr}}{v_e}}, \quad (6)$$

where a_d and ρ_d are the average size and density of a dust grain, respectively.

When solving the energy balance equation free parameters describing the dust, i.e., via the dust-gas collisional heating, are introduced. These are highly uncertain, but affect the derived line intensities. Here we assume that the Q -parameter, i.e., the efficiency of momentum transfer, to be equal to 0.03 [for details see Habing et al. (1994)], and define a new parameter that contains the other dust parameters,

$$h = \left(\frac{\Psi}{0.01} \right) \left(\frac{2.0 \text{ g cm}^{-3}}{\rho_d} \right) \left(\frac{0.05 \mu\text{m}}{a_d} \right), \quad (7)$$

where the normalized values are the ones we used to fit the CO line emission of CW Leo using our model, i.e., $h=1$ for this object.

Additional heating is provided by the photoelectric effect (Huggins et al. 1988)

$$H_{pe} = k_{pe} n_{H_2}, \quad (8)$$

where k_{pe} is a constant that depends on the properties of the dust grains. Following Huggins et al. (1988) we adopt $k_{pe}=1 \times 10^{-26} \text{ erg s}^{-1}$. This heating mechanism is important in the cool, tenuous, outer parts of CSEs around high mass loss rate stars.

The spatial extent of the molecular envelope is generally an important input parameter, and the derived mass loss rate will depend on this. The radial distribution of CO in the CSE was estimated using the modelling presented in Mamon et al. (1988). It includes photodissociation, taking into account the effects of dust-, self- and H₂-shielding, and chemical exchange reactions. Mamon et al. (1988) find that the radial abundance distribution of CO with respect to H₂, $f(r)$, can be described by

$$f(r) = f_0 \exp \left[-\ln 2 \left(\frac{r}{r_p} \right)^\alpha \right], \quad (9)$$

where f_0 is the initial (photospheric) abundance, r_p is the photodissociation radius (where the abundance has dropped to $f_0/2$), and α is a parameter describing the rate at which the abundance declines. Both r_p and α depend on the mass loss rate (\dot{M}), the expansion velocity (v_e), and f_0 . In our modelling we use analytical fits to these results from Stanek et al. (1995)

$$r_p = 5.4 \times 10^{16} \left(\frac{\dot{M}}{10^{-6}} \right)^{0.65} \left(\frac{v_e}{15} \right)^{-0.55} \left(\frac{f_0}{8 \times 10^{-4}} \right)^{0.55} + 7.5 \times 10^{15} \left(\frac{v_e}{15} \right) \text{ cm} \quad (10)$$

and Kwan & Webster (1993)

$$\alpha = 2.79 \left(\frac{\dot{M}}{10^{-6}} \right)^{0.09} \left(\frac{15}{v_e} \right)^{0.09}, \quad (11)$$

where the units of \dot{M} and v_e are $\text{M}_\odot \text{yr}^{-1}$ and km s^{-1} , respectively. In what follows we will assume $f_0=1 \times 10^{-3}$. This is an

average of the f_0 :s estimated by Olofsson et al. (1993b) for this sample of optically bright carbon stars. The scatter in the estimated f_0 :s is about 40%. We note here that a somewhat more sophisticated photodissociation model was developed by Doty & Leung (1998) in which they include scattering by dust. For the CSE of CW Leo they derive a CO envelope size which is 30% smaller than what is obtained using the Mamon et al. model. It is however not clear by how much the envelope size changes for an object with a significantly lower mass loss rate, and hence we use the results of Mamon et al. here.

In our models we include both a central source of radiation and the cosmic microwave background radiation at 2.7 K. The central radiation emanates from the star, and was estimated from a fit to its spectral energy distribution (SED), usually by assuming two blackbodies. This method is described in Kerschbaum (1999). A fit to the SED gives the two blackbody temperatures, T_* and T_d , and the relative luminosities of the two blackbodies, L_d/L_* . Any dust present around the star will absorb parts of the stellar light and re-emit it at longer wavelengths. Thus, of the two blackbodies used, one represents the stellar contribution and one represents the dust. However, it should be noted that, e.g., the stellar temperature T_* derived in this manner is generally lower than the true temperature of the star (Kerschbaum 1999). In any case, the two blackbodies used give a good description of the radiation that the CSE is subjected to. The temperatures and luminosities used in the modelling are presented in Table 3. Only in the cases where $L_d/L_* > 0.1$ the dust component was retained. The inner boundary of the CSE, r_i , was set to reside outside the radius of the central blackbody(s), but never lower than 1×10^{14} cm ($\sim 3 R_\odot$), i.e., generally beyond both the sonic point and dust condensation radius.

The distances, presented in Table 3, were estimated using one of the following methods: the observed Hipparcos parallax, a period-luminosity relation (Groenewegen & Whitelock 1996), or an assumed bolometric luminosity. In the two former cases the luminosities were estimated using apparent bolometric magnitudes and the distances. In the rare cases when both the distance obtained from Hipparcos and the period-luminosity relation result in extremely high or low luminosities, a value of $4000 L_\odot$ was adopted as the luminosity and the distance was estimated using this value. For the irregular variables with no Hipparcos data we also assumed a luminosity of $4000 L_\odot$. For a statistical study of a large sample of stars these distance estimates are adequate, although the distance estimate for an individual star has a large uncertainty. There is no apparent systematic difference between the distances derived from the period-luminosity relation and the Hipparcos parallaxes, Fig. 2. The distances in Olofsson et al. (1993a) were estimated from an adopted absolute K magnitude. The distances presented here are systematically lower by, on the average, a factor of 1.4 than those used in Olofsson et al.

This was a summary of the assumptions used in "the standard model". In what follows, tests will be made to see how sensitive the model is to the various assumptions.

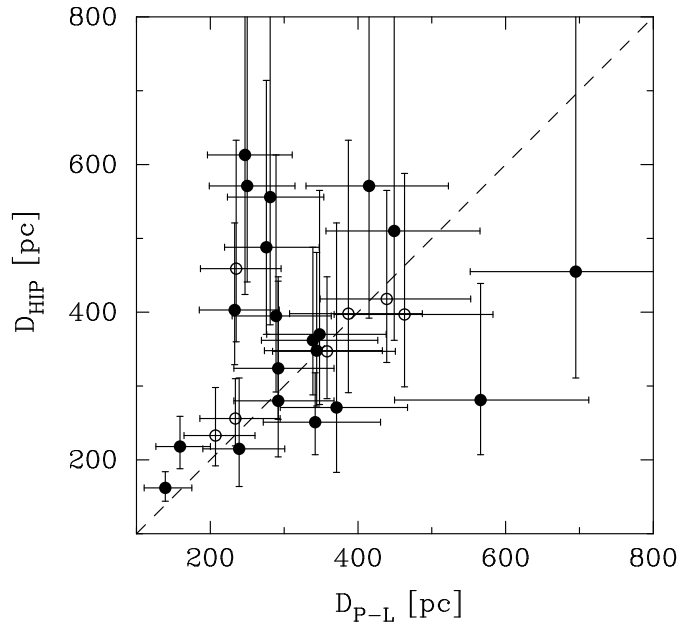


Fig. 2. Comparison between the distances derived from the period-luminosity relation (D_{P-L}) and the Hipparcos parallaxes (D_{HIP}). The irregular variables where the luminosity was assumed to equal $4000 L_\odot$ are indicated by open circles. The dashed line shows the 1:1 correlation.

4. Model results

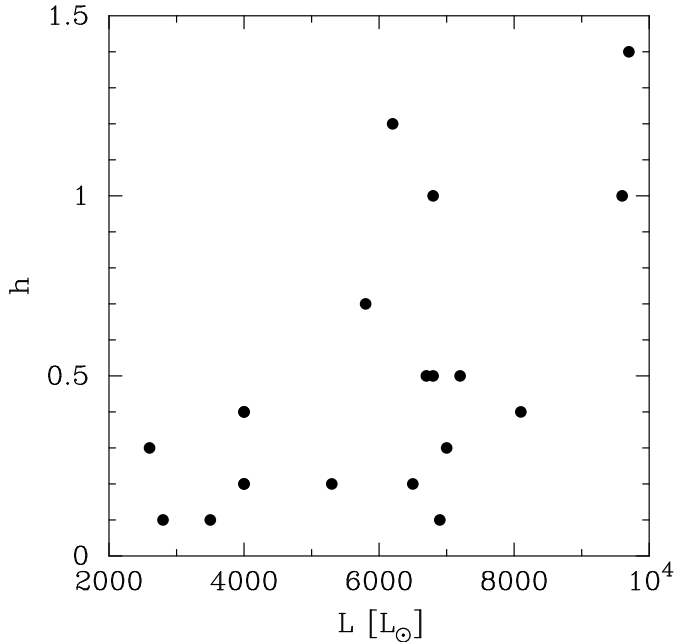


Fig. 3. The h -parameter derived from the radiative transfer analysis plotted against the adopted luminosity of the central star. Note that the data points at $L=4000 L_\odot$ represent two stars each.

Table 3. Input parameters and CO modelling results using the standard model (see text for details)

Source	Var. type	P [days]	D [pc]	L [L_{\odot}]	T_* [K]	T_d^6 [K]	L_d/L_*^6	\dot{M} [M_{\odot} yr $^{-1}$]	v_e [km s $^{-1}$]	r_p [cm]	h
VX And	SRa	369	560 ²	5500	2000			4.0×10^{-8}	11.5	1.4×10^{16}	0.2 ⁴
HV Cas	M	527	970 ²	7900	1800	900	0.54	9.0×10^{-7}	18.5	6.1×10^{16}	0.5 ⁴
IRC+60041			670 ³	4000	1300	500	0.13	3.0×10^{-6}	28.0	1.0×10^{17}	0.2 ⁴
Z Psc	SRb	144	320 ¹	3100	2600			2.5×10^{-8}	3.5	1.4×10^{16}	0.2 ⁴
R For	M	389	610 ²	5800	1500	700	0.52	1.3×10^{-6}	16.5	8.0×10^{16}	0.7
TW Hor	SRb	158	400 ¹	6700	2600			9.0×10^{-8}	5.5	2.5×10^{16}	0.5
V384 Per	M	535	560 ²	8100	1900	900	10	3.5×10^{-6}	15.0	1.4×10^{17}	0.4
V466 Per	SR		450 ³	4000	2200			1.3×10^{-7}	9.0	2.6×10^{16}	0.2 ⁴
ST Cam	SRb	300	330 ²	4400	1600			9.0×10^{-8}	9.0	2.1×10^{16}	0.2 ⁴
TT Tau	SRb	167	360 ²	2400	2400			7.0×10^{-8}	5.0	2.2×10^{16}	0.2 ⁴
R Lep	M	467	250 ¹	4000	1900	800	0.14	7.0×10^{-7}	18.0	5.3×10^{16}	0.2
W Ori	SRb	212	220 ¹	2600	2200			7.0×10^{-8}	11.0	1.8×10^{16}	0.3
S Aur	SR	590	820 ²	8900	1600	700	0.32	2.2×10^{-6}	25.5	8.9×10^{16}	0.5 ⁴
W Pic	Lb		490 ³	4000	2000			3.0×10^{-7}	16.0	3.5×10^{16}	0.4
Y Tau	SRb	242	310 ²	3500	2400			4.0×10^{-7}	11.0	4.5×10^{16}	0.1
TU Gem	SRb	230	330 ²	3400	2400			2.5×10^{-7}	11.5	3.4×10^{16}	0.2 ⁴
BL Ori	Lb		360 ³	4000	2700			1.1×10^{-7}	9.0	2.4×10^{16}	0.2 ⁴
UU Aur	SRb	234	260 ²	6900	2500			3.5×10^{-7}	11.0	4.2×10^{16}	0.1
NP Pup	Lb		420 ¹	3500	2700			6.5×10^{-8}	9.5	1.8×10^{16}	0.2 ⁴
CL Mon	M	497	770 ²	7500	2000	1100	1.4	2.2×10^{-6}	25.0	8.9×10^{16}	0.5 ⁴
RY Mon	SRa	456	456 ¹	3000	2000			3.5×10^{-7}	11.0	4.2×10^{16}	0.2 ⁴
W CMa	Lb		450 ³	4000	2500			3.0×10^{-7}	10.5	3.9×10^{16}	0.2 ⁴
R Vol	M	454	730 ²	6800	1300	800	0.7	1.8×10^{-6}	18.0	9.0×10^{16}	1.0
X Cnc	SRb	195	280 ²	2800	2200			1.0×10^{-7}	7.0	2.4×10^{16}	0.1
CW Leo	M	630	120 ²	9600		510		1.5×10^{-5}	14.5	3.7×10^{17}	1.0
Y Hya	SRb	303	350 ¹	4200	2600			1.9×10^{-7}	9.0	3.2×10^{16}	0.2 ⁴
X Vel	SR	140	310 ²	2800	2200			1.8×10^{-7}	10.0	3.0×10^{16}	0.2 ⁴
SZ Car	SRb	126	580 ³	4000	2400			2.0×10^{-6}	14.0	1.1×10^{17}	0.2
RW LMi	SRa	640	440 ²	9700	1300	510	6.7	6.0×10^{-6}	17.0	1.9×10^{17}	1.4
XZ Vel			530 ³	4000	1900			6.0×10^{-7}	14.0	5.2×10^{16}	0.2 ⁴
CZ Hya	M	442	960 ²	6600	1800			9.0×10^{-7}	12.0	7.0×10^{16}	0.5 ⁴
CCS 2792			480 ³	4000	2000			6.5×10^{-7}	17.0	5.2×10^{16}	0.2 ⁴
U Hya	SRb	450	160 ¹	2500	2400			1.4×10^{-7}	7.0	2.9×10^{16}	0.2 ⁴
VY UMa	Lb		330 ³	4000	2700			7.0×10^{-8}	6.0	2.1×10^{16}	0.2 ⁴
SS Vir	SRa	364	540 ²	5400	1800			2.0×10^{-7}	12.5	3.0×10^{16}	0.2 ⁴
Y CVn	SRb	157	220 ¹	4400	2200			1.5×10^{-7}	8.5	2.9×10^{16}	0.2 ⁵
RY Dra	SRb:	200	490 ¹	10000	2500			3.0×10^{-7}	10.0	4.0×10^{16}	1.2 ⁵
HD 121658			530 ³	4000	2400			1.0×10^{-7}	6.5	2.5×10^{16}	0.2 ⁴
HD 124268			390 ³	4000	2300			1.0×10^{-7}	11.0	2.2×10^{16}	0.2 ⁴
X TrA	Lb		460 ³	4000	2200			1.3×10^{-7}	8.0	2.7×10^{16}	0.4
V CrB	M	358	630 ²	5300	1900	740	0.15	6.0×10^{-7}	7.5	6.8×10^{16}	0.2
TW Oph	SRb	185	280 ¹	2700	2000			5.0×10^{-8}	7.5	1.6×10^{16}	0.2 ⁴
T Dra	M	422	610 ²	6300	1600	650	0.28	1.2×10^{-6}	13.5	8.0×10^{16}	0.5 ⁴
T Lyr	Lb		340 ³	4000	2000			7.0×10^{-8}	11.5	1.8×10^{16}	0.5 ⁵
V Aql	SRb	353	370 ¹	6500	2100			3.0×10^{-7}	8.5	4.2×10^{16}	0.2
V1942 Sgr	Lb		430 ³	4000	2600			1.6×10^{-7}	10.0	2.8×10^{16}	0.2 ⁴
UX Dra	SRa:	168	310 ³	4000	2600			1.6×10^{-7}	4.0	4.0×10^{16}	0.2 ⁴
AQ Sgr	SRb	200	420 ³	4000	2700			2.5×10^{-7}	10.0	3.6×10^{16}	0.2 ⁴
RT Cap	SRb	393	450 ²	5900	2200			1.0×10^{-7}	8.0	2.3×10^{16}	0.2 ⁴
U Cyg	M	463	710 ²	6900	2200			9.0×10^{-7}	13.0	6.8×10^{16}	0.5 ⁴
V Cyg	M	421	370 ²	6200	1500	860	0.84	1.2×10^{-6}	11.5	8.5×10^{16}	1.2
RV Aqr	M	454	670 ²	6800	1300	620	0.46	2.5×10^{-6}	16.0	1.1×10^{17}	0.5
T Ind	SRb	320	570 ¹	8800	2600			9.0×10^{-8}	6.0	2.4×10^{16}	0.5 ⁴
Y Pav	SRb	233	360 ²	4100	2400			1.6×10^{-7}	8.0	3.0×10^{16}	0.2 ⁴
V1426 Cyg	M	470	780 ²	7100	1200	580	0.5	1.0×10^{-5}	14.0	2.9×10^{17}	0.3
S Cep	M	487	340 ²	7300	1400			1.5×10^{-6}	22.0	7.5×10^{16}	0.4

Table 3. continued.

Source	Var. type	P [days]	D [pc]	L [L_{\odot}]	T_* [K]	T_d^6 [K]	L_d/L_*^6	\dot{M} [M_{\odot} yr $^{-1}$]	v_e [km s $^{-1}$]	r_p [cm]	h
V460 Cyg	SRb	180	230 ²	2600	2800			1.8×10^{-7}	10.0	3.0×10^{16}	0.2 ⁴
RV Cyg	SRb	263	310 ²	3400	2100			4.5×10^{-7}	13.5	4.5×10^{16}	0.2 ⁴
PQ Cep	M		390 ²	4000	1700	840	0.13	1.4×10^{-6}	19.5	7.6×10^{16}	0.2 ⁴
LP And	M	620	630 ²	9400	1100	610	6.6	1.5×10^{-5}	14.0	4.0×10^{17}	0.7
WZ Cas	SRb	186	290 ²	2700	2500			6.5×10^{-9}	2.5	7.4×10^{15}	0.2 ⁴

¹ Hipparcos; ² Period-luminosity relation (Groenewegen & Whitelock 1996); ³ $L=4000 L_{\odot}$ assumed; ⁴ Assumed h -parameter (see text for details); ⁵ J-type star (only including ^{12}CO cooling); ⁶ In the cases when $L_d/L_* < 0.1$ the dust blackbody component was not retained and a single blackbody representing the stellar component adequately describes the SED. In the case of CW Leo a single dust blackbody is used to represent the SED.

4.1. The fitting strategy

With the assumptions made in the standard model there remains two principal free parameters, the mass loss rate (\dot{M}) and the h -parameter. These two parameters were allowed to vary simultaneously, \dot{M} in steps of $\sim 10\%$ and h in somewhat larger steps, until the model with the smallest deviations from the observed intensities was found. The quality of a particular model with respect to the observational constraints can be quantified using the chi-square statistic defined as

$$\chi^2 = \sum_{i=1}^N \frac{[I_{\text{mod},i} - I_{\text{obs},i}]^2}{\sigma_i^2}, \quad (12)$$

where I is the total integrated line intensity, σ_i is the uncertainty in observation i , and the summation is done over all independent observations N . The errors in the observed intensities are generally dominated by the calibration uncertainty of $\sim 20\%$. In some cases the line profiles were used to discriminate between models. For each new \dot{M} assigned, a consistent envelope size (r_p) was calculated based upon the results of Mamom et al. (1988).

It is found that the intensity ratios between the different lines are sensitive to various parameters, and hence can be used to constrain them (Sec. 4.3). Therefore, in order to accurately determine h , and ultimately \dot{M} , multi-transition observations are needed. Observed radial brightness profiles provide additional important information. For a limited number of the sources in our sample there are enough observational constraints that a reliable h -parameter may be estimated. These sources were first modelled, see Table 3.

4.2. The h -parameter

The derived h -parameters, as a function of the adopted luminosity of the central source, are shown in Fig. 3. A division between low luminosity objects and those with higher luminosities is evident. For luminosities lower than $6000 L_{\odot}$ the median value of the estimated h -parameter is 0.2 (based on 9 sources), while for the higher luminosities it is 0.5 (12 sources) (the J-type stars, i.e., stars with a high content of ^{13}CO , were not included in these estimates since ^{13}CO line cooling is not treated in the standard model). The large scatter for the high

luminosity sources is unfortunate, since these are generally the sources where the derived mass loss rates are particularly sensitive to the adopted value of h . For the majority of objects, where a reliable estimate of the h -parameter is not possible, we have adopted a value of $h=0.2$ for the low luminosity objects (below $6000 L_{\odot}$) and $h=0.5$ for the high luminosity objects (above $6000 L_{\odot}$).

The h -parameter is related to the dust-to-gas mass ratio, Ψ (see Eq. 7). If we assume that the properties of a dust grain are equal to those used to fit the line emission from CW Leo, and that they are the same for all stars, an h -parameter of 0.2 means that $\Psi=2 \times 10^{-3}$. Groenewegen et al. (1998b) have modelled the dust emission towards a large sample of carbon stars and find a value of Ψ which is fairly constant at 2.5×10^{-3} for stars with luminosities up to about $7900 L_{\odot}$, and which increases drastically with luminosity up to 0.01 and higher. This is in good agreement with our results and lends further support to our distinction between low- and high-luminosity stars as regards the value of the h -parameter. Furthermore, Hiriart & Kwan (2000) derive, for 17 of our sample stars, on the average $\Psi \sim 7 \times 10^{-4}$. The main reason for this discrepancy is the difference in the adopted dust parameters. In fact, it can be shown that for $h=0.2$ we get essentially the same heating term (cf. Eq. 6) in the energy balance equation as Hiriart & Kwan (2000).

4.3. The mass loss rates

We have managed to model reasonably well 61 of the 69 sample sources using our standard model and fitting strategy defined above. The reduced χ^2 for these models is estimated from

$$\chi_{\text{red}}^2 = \frac{\chi_{\text{min}}^2}{N - p}, \quad (13)$$

where χ_{min}^2 is obtained from Eq. 12 for the best fit model, and p is the number of adjustable parameters (one or two) in the model. Typically, $\chi_{\text{red}}^2 \sim 1-3$ assuming a calibration uncertainty of 20%. The derived mass loss rates and h -parameters are presented in Table 3, where also the velocities by which the CSEs expand, v_e , and their spatial extents, r_p , are given.

The derived mass loss rates presented in Table 3 span more than three orders of magnitude, $6.5 \times 10^{-9} M_{\odot} \text{ yr}^{-1}$ to

Table 4. CO modelling results compared to single dish observations.

Source	Tel.	Trans.	I_{obs} [K km s $^{-1}$]	I_{mod} [K km s $^{-1}$]	Ref.	Source	Tel.	Trans.	I_{obs} [K km s $^{-1}$]	I_{mod} [K km s $^{-1}$]	Ref.
VX And	OSO	1–0	<0.8	0.1	2	UU Aur	OSO	1–0	7.9	8.2	2
	IRAM	1–0	<1.4	0.2	2		IRAM	1–0	18.8	16.9	2
	IRAM	2–1	2.4	2.4	2		JCMT	2–1	16.8	14.8	4
HV Cas	OSO	1–0	<2.1	1.9	2	NP Pup	IRAM	2–1	39.0	46.2	2
	IRAM	1–0	5.6	4.1	2		SEST	1–0	<0.5	0.3	2
	IRAM	2–1	11.9	14.5	2		SEST	2–1	1.2	1.2	2
IRC+60041	IRAM	1–0	IS	4.7	2	CL Mon	SEST	1–0	3.2	3.3	2
	IRAM	2–1	17.3	17.3	2		SEST	2–1	10.4	9.5	2
	OSO	1–0	1.0	0.7	2		IRAM	2–1	34.3	38.1	2
Z Psc	IRAM	1–0	2.1	1.6	2	RY Mon	IRAM	1–0	6.8	5.4	2
	IRAM	2–1	4.6	6.0	2		IRAM	2–1	11.3	14.5	2
	SEST	1–0	4.8	4.9	2		SEST	1–0	1.3	1.3	2
R For	SEST	2–1	11.0	14.5	2	W CMa	SEST	2–1	4.6	3.9	2
	JCMT	2–1	21.0	17.3	4		IRAM	2–1	11.7	16.0	2
	SEST	3–2	18.0	19.9	1		SEST	1–0	4.9	5.1	2
	JCMT	3–2	27.4	25.6	4		SEST	2–1	15.3	14.7	2
	SEST	1–0	1.0	0.9	2		SEST	3–2	21.0	22.2	1
TW Hor	SEST	2–1	3.3	3.8	2	X Cnc	NRAO	1–0	0.7	0.7	1
	SEST	3–2	7.2	6.1	1		SEST	1–0	1.5	1.1	2
	NRAO	1–0	7.8	10.1	1		OSO	1–0	1.7	2.0	2
V384 Per	OSO	1–0	25.5	25.1	2	CW Leo	SEST	2–1	3.2	2.9	2
	IRAM	1–0	52.7	48.4	2		IRAM	2–1	11.1	11.8	2
	JCMT	2–1	37.3	35.2	4		NRAO	1–0	170.8	257.1	1
	IRAM	2–1	83.6	102.0	2		SEST	1–0	288.1	305.3	2
	JCMT	3–2	44.5	42.5	4		OSO	1–0	422.0	391.7	2
V466 Per	IRAM	1–0	3.6	2.5	2	CW Leo	SEST	2–1	487.3	580.5	2
	IRAM	2–1	6.2	8.6	2		JCMT	2–1	731.8	632.2	4
ST Cam	OSO	1–0	2.0	2.0	2	CW Leo	IRAM	2–1	1057.7	1116.1	2
	JCMT	2–1	3.4	4.4	4		SEST	3–2	854.8	774.0	1
TT Tau	IRAM	2–1	15.2	14.8	2	CW Leo	JCMT	3–2	1066.3	883.7	4
	IRAM	1–0	2.6	2.7	2		JCMT	4–3	1227.8	1052.0	4
R Lep	IRAM	2–1	4.0	8.1	2	Y Hya	SEST	1–0	1.6	1.6	2
	SEST	1–0	6.2	6.7	2		IRAM	2–1	18.7	19.4	2
	IRAM	1–0	31.7	24.3	2		SEST	1–0	1.4	1.5	2
	SEST	2–1	18.1	17.4	2		SEST	2–1	4.3	4.4	2
	IRAM	2–1	56.4	64.2	2		SZ Car	SEST	1–0	2.8	2.7
W Ori	SEST	3–2	12.5	21.6	2		SEST	2–1	7.8	5.9	2
	JCMT	3–2	28.1	27.9	4		SEST	3–2	5.9	6.2	1
	SEST	1–0	1.2	1.3	2		NRAO	1–0	36.4	37.0	1
	OSO	1–0	2.7	2.4	2		SEST	1–0	54.6	51.9	2
	IRAM	1–0	5.0	5.1	2		OSO	1–0	87.0	83.8	2
S Aur	SEST	2–1	4.9	4.3	2	RW LMi	SEST	2–1	105.4	128.4	2
	IRAM	2–1	19.0	16.9	2		JCMT	2–1	163.2	147.4	4
	SEST	3–2	4.8	5.4	1		JCMT	3–2	245.3	208.6	4
	OSO	1–0	6.7	5.5	2		JCMT	4–3	243.1	224.3	4
	IRAM	1–0	10.9	11.9	2		SEST	1–0	1.8	1.4	2
W Pic	IRAM	2–1	15.8	36.8	2	XZ Vel	SEST	2–1	3.5	4.1	2
	SEST	1–0	0.9	0.9	2		SEST	1–0	1.5	1.5	2
Y Tau	SEST	2–1	2.6	3.1	2	CZ Hya	SEST	2–1	4.2	4.5	2
	SEST	3–2	6.1	4.5	1		SEST	1–0	1.9	1.8	2
	SEST	1–0	3.2	3.0	2		SEST	2–1	4.1	4.7	2
	OSO	1–0	6.3	5.3	2		SEST	1–0	5.4	5.4	2
	IRAM	1–0	15.5	11.0	2		SEST	2–1	13.8	14.1	1
TU Gem	SEST	2–1	5.8	6.1	2	CCS 2792	JCMT	2–1	20.2	16.6	4
	IRAM	2–1	19.4	24.1	2		SEST	1–0	48.8	48.7	4
	OSO	1–0	3.4	3.4	2		SEST	2–1	4.3	11.0	2
	IRAM	1–0	6.5	21.1	2		SEST	1–0	7.9	8.5	2
BL Ori	OSO	1–0	IS	1.2	2	VY UMa	OSO	1–0	<1.2	1.1	2
	IRAM	1–0	IS	2.6	2		IRAM	1–0	1.4	1.4	2
	IRAM	2–1	9.8	9.7	2		OSO	1–0	1.4	1.4	2
SS Vir	OSO	1–0	IS	1.2	2		IRAM	1–0	4.3	11.0	2
	IRAM	1–0	IS	2.6	2		IRAM	1–0	7.9	8.5	2

Table 4. continued.

Source	Tel.	Trans.	I_{obs} [K km s $^{-1}$]	I_{mod} [K km s $^{-1}$]	Ref.	Source	Tel.	Trans.	I_{obs} [K km s $^{-1}$]	I_{mod} [K km s $^{-1}$]	Ref.
Y CVn	OSO	1–0	4.5	5.4	2	V Cyg	OSO	1–0	27.5	27.2	2
	IRAM	1–0	10.3	11.2	2		NRAO	2–1	50.1	36.5	1
	JCMT	2–1	11.9	10.9	4		JCMT	2–1	35.9	56.2	4
	IRAM	2–1	22.7	34.2	2		JCMT	3–2	88.9	86.1	4
	JCMT	3–2	20.9	15.6	4		JCMT	4–3	123.4	95.2	4
RY Dra	OSO	1–0	2.4	3.0	2	RV Aqr	SEST	1–0	7.5	6.9	2
	IRAM	2–1	21.6	28.3	2		SEST	2–1	18.1	17.2	2
	JCMT	3–2	18.9	15.8	4		SEST	3–2	18.6	20.5	1
HD 121658	SEST	1–0	1.5	1.4	2	T Ind	SEST	1–0	0.5	0.4	2
HD 124268	SEST	1–0	<0.7	0.6	2		SEST	2–1	1.5	1.9	2
X TrA	SEST	2–1	2.1	1.9	2	Y Pav	SEST	1–0	1.6	1.4	2
	SEST	1–0	2.5	2.7	2		SEST	2–1	3.8	4.3	2
	SEST	2–1	11.8	10.2	2		OSO	1–0	17.3	17.0	2
V CrB	SEST	3–2	15.3	15.1	1		SEST	2–1	8.7	14.3	2
	OSO	1–0	2.7	3.9	2	V1426 Cyg	SEST	3–2	17.8	17.1	1
	IRAM	1–0	11.4	8.4	3		OSO	1–0	16.3	19.4	2
TW Oph	IRAM	2–1	18.4	18.8	2		IRAM	1–0	48.5	38.1	3
	SEST	1–0	1.1	0.9	2		JCMT	2–1	49.3	37.3	4
	IRAM	2–1	8.7	10.2	2		IRAM	2–1	76.6	109.6	2
T Dra	OSO	1–0	8.8	8.4	2	S Cep	JCMT	3–2	55.7	55.4	4
	IRAM	1–0	28.6	17.7	3		JCMT	4–3	65.7	60.0	4
	IRAM	2–1	43.7	48.7	2		OSO	1–0	4.7	4.8	2
T Lyr	OSO	1–0	0.7	1.0	2	V460 Cyg	IRAM	2–1	8.5	28.4	2
	IRAM	2–1	5.6	9.6	2		OSO	1–0	4.8	6.1	2
	JCMT	3–2	6.4	4.3	4		IRAM	1–0	16.7	12.9	2
V Aql	SEST	1–0	2.8	2.6	2	RV Cyg	IRAM	2–1	14.4	33.5	2
	OSO	1–0	3.2	4.8	2		OSO	1–0	6.4	6.7	2
	SEST	2–1	8.1	7.0	2		NRAO	2–1	8.7	7.4	1
	JCMT	2–1	9.0	8.3	4	LP And	OSO	1–0	57.0	58.8	1
	JCMT	3–2	11.2	10.6	4		IRAM	1–0	92.7	97.4	3
V1942 Sgr	SEST	1–0	0.8	0.8	2	PQ Cep	NRAO	2–1	60.7	46.5	1
	OSO	1–0	2.1	1.7	2		JCMT	2–1	90.6	68.5	4
UX Dra	IRAM	2–1	6.8	9.0	2	WZ Cas	IRAM	2–1	155.8	166.8	3
	SEST	1–0	1.4	1.3	2		JCMT	3–2	88.0	79.1	4
	SEST	2–1	4.1	4.0	2		JCMT	4–3	73.3	78.6	4
AQ Sgr	SEST	1–0	0.6	0.6	2		OSO	1–0	<1.1	0.1	2
	SEST	2–1	2.0	2.1	2		IRAM	1–0	<2.6	0.3	2
RT Cap	OSO	1–0	4.9	4.8	2		IRAM	2–1	2.6	2.8	2
	IRAM	2–1	9.4	31.7	2						

1. This paper; 2. Olofsson et al. (1993a); 3. Neri et al. (1998); 4. JCMT public archive.

$1.5 \times 10^{-5} M_{\odot} \text{ yr}^{-1}$, over which the physical conditions of the CSEs vary considerably, posing a challenge to the model. The intensities, overall line shapes, and when available radial brightness distributions, of the circumstellar CO lines produced by the radiative transfer model generally agree well with those observed. This is illustrated here for three of our sample stars LP And (Fig. 4), R For (Fig. 5), and W Ori (Fig. 6). These carbon stars span a large range in mass loss rate and serve to illustrate the various physical conditions in these CSEs.

A full, detailed, error analysis of the estimated mass loss rates is not possible due to the relatively large number of free parameters entering the model. Instead, we will vary some of

the more important parameters in order to illustrate the sensitivity of the model, and to be able to get a rough estimate of the errors involved in the mass loss rate estimates. The results of these sensitivity tests are shown in Table 5 for our three example stars. In addition, in Fig. 7 we present chi-square contour plots for these stars, produced by varying the mass loss rate and the h -parameter. This will give an estimate of the accuracy in the determination of these two adjustable parameters when all other parameters are held fixed (the size and shape of the CO envelope is however allowed to change in accordance with Eqs 10 and 11). In Fig. 7 we indicate various confidence levels with the contour at $\chi^2_{\text{min}} + 2.3$ marking the 68% confi-

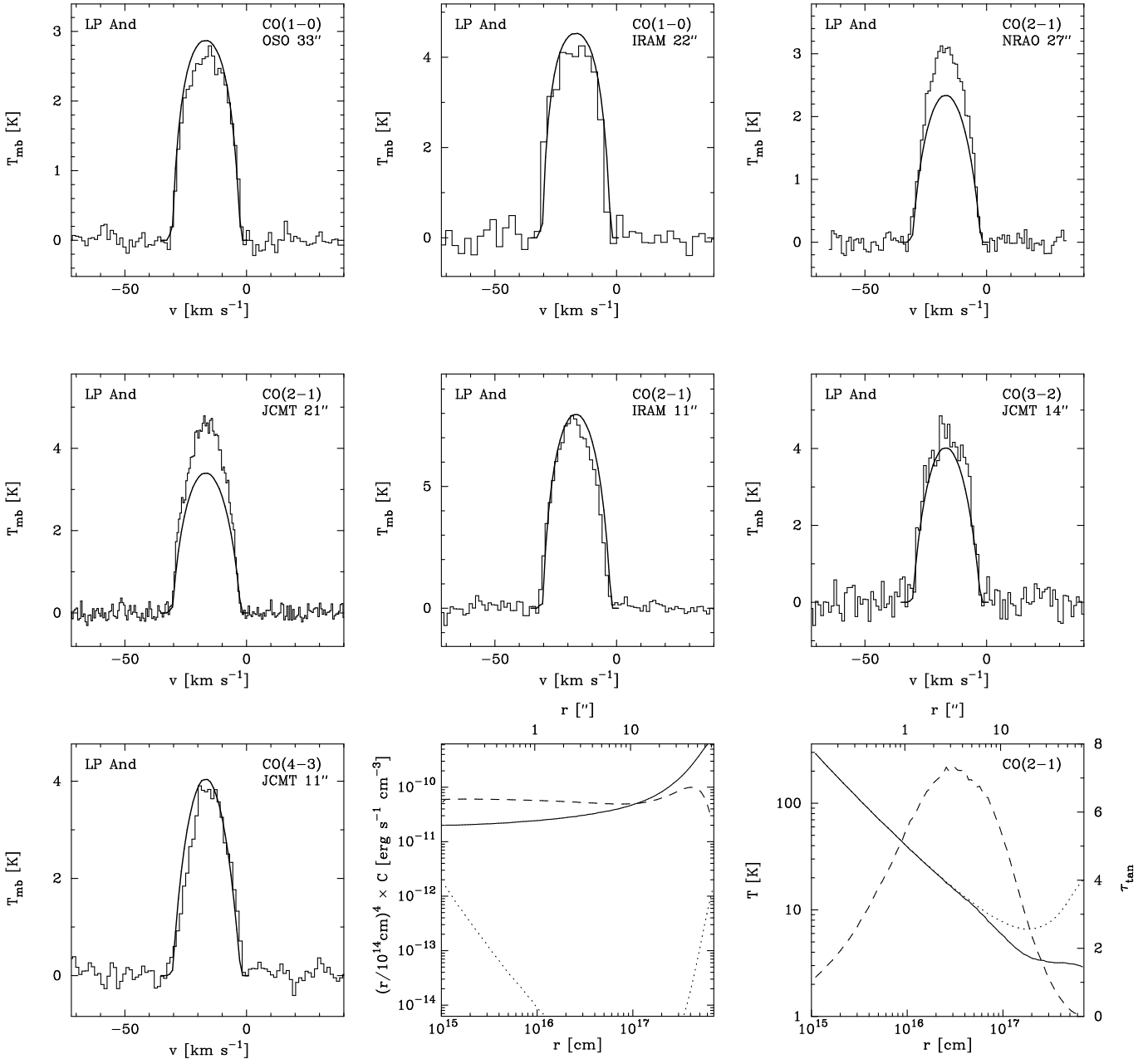


Fig. 4. Multi-transition CO millimetre-wave line emission observed towards the high mass loss rate Mira variable LP And. The observed spectra (histograms) have been overlayed with the model prediction (full line) using a mass loss rate of $1.5 \times 10^{-5} M_{\odot} \text{ yr}^{-1}$. The transition, telescope used, and the corresponding beamsize, are indicated for each of the observations. *Cooling panel:* The full line represents adiabatic cooling; the dotted line gives the H_2 cooling; and the dashed line is CO cooling (see text for details). *Temperature/optical-depth panel:* The dotted line shows the kinetic gas temperature derived from the energy balance equation. The full line gives the excitation temperature of the CO($J=2 \rightarrow 1$) transition. The dashed lines give the tangential optical depth, τ_{\tan} , of the CO($J=2 \rightarrow 1$) transition.

dence limit (i.e., the "1 σ " level for two adjustable parameters). The information contained in the shape of the line profiles (to which the χ^2 defined above is not very sensitive) have occasionally been used to further constrain the most probable parameter space.

LP And is a high mass loss rate Mira variable where the excitation of ^{12}CO is dominated by collisions. Consequently, the

line intensities are very sensitive to the temperature structure, i.e., the h -parameter. It is interesting to note that the assumed envelope size r_p does not significantly affect the derived mass loss rate in the high mass loss rate regime. The reason for this being that the density is too low to excite the CO molecules effectively (the lines are sub-thermally excited) in the cool outer parts of the envelope (cf. Fig. 4), i.e., the emission is excitation

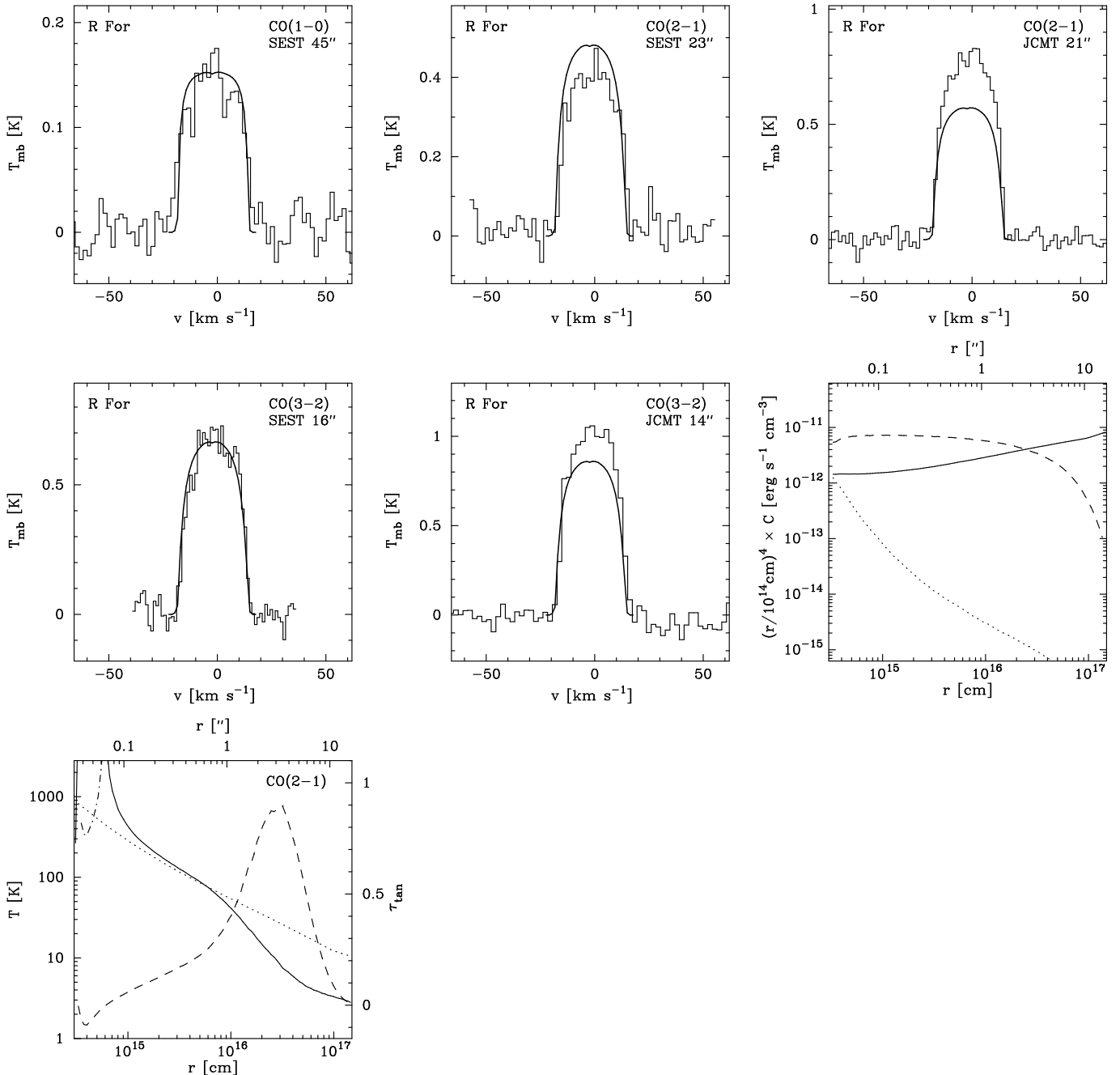


Fig. 5. Multi-transition CO millimetre-wave line emission observed towards the bright carbon star R For. The observed spectra (histograms) have been overlayed with the model prediction (full line) using a mass loss rate of $1.3 \times 10^{-6} M_{\odot} \text{ yr}^{-1}$. The transition, telescope used, and the corresponding beamsize, are indicated for each of the observations. *Cooling panel:* The full line represents adiabatic cooling; the dotted line gives the H_2 cooling; and the dashed line is CO cooling (see text for details). *Temperature/optical-depth panel:* The dotted line shows the kinetic gas temperature derived from the energy balance equation. The full line gives the excitation temperature of the $\text{CO}(J=2 \rightarrow 1)$ transition, and a dash-dot line indicates a negative excitation temperature, i.e., maser action. The dashed lines give the tangential optical depth, τ_{tan} , of the $\text{CO}(J=2 \rightarrow 1)$ transition.

limited. In the high mass loss rate regime the line intensities are also insensitive to the adopted mass loss rate since an increase in \dot{M} leads to more cooling ($C \propto \dot{M}$ while $H \propto \dot{M}^{0.5}$), which compensates for the increase of molecular density. This "saturation"-effect of the line intensities for high mass loss

rates has been noted before in other models where the cooling by CO is treated in a self-consistent manner (Sahai 1990; Kastner 1992). Additional sensitivity tests in the case of a high mass loss rate object (CW Leo) can be found in Groenewegen (1994).

Table 5. The effect on the integrated model intensity I_{mod} (in percent), obtained by SEST and JCMT, due to changes in various parameters. In general, the accuracy of the observed intensities lie at the $\pm 20\%$ level.

Parameter	Change	LP And				R For				W Ori			
		1-0	2-1	3-2	4-3	1-0	2-1	3-2	4-3	1-0	2-1	3-2	4-3
$\dot{M}^{1,2}$	+50%	+25	+15	+15	+10	+50	+55	+55	+55	-10	+15	+40	+55
	-33%	-25	-15	-15	-15	-35	-35	-40	-40	-40	-30	-25	-35
\dot{M}	+50%	+15	0	0	+5	+55	+40	+35	+30	+25	+30	+40	+45
	-33%	-15	-5	-5	-5	-35	-30	-30	-25	-40	-25	-20	-30
L^1	+50%	0	0	0	0	0	0	0	0	+15	+10	+5	+5
	-33%	0	0	0	0	0	-5	0	0	-20	-10	-5	-5
h	+50%	+25	+35	+35	+40	+10	+15	+20	+25	0	+5	+10	+15
	-33%	-20	-25	-30	-30	-10	-15	-20	-20	0	-10	-10	-15
r_p	+50%	+5	0	0	0	+15	+5	+5	0	+20	+5	+5	0
	-33%	-5	0	0	0	-20	-5	0	0	-50	-30	-10	-5
r_i	$\times 2$	+5	0	0	0	+5	+5	+5	0	+5	+15	+15	+10
v_t	$\times 2$	+10	0	0	0	+15	+10	+5	+5	0	+25	+40	+30

¹ Same temperature structure as final model was used; ²Same envelope size as final model was used.

W Ori, on the other hand, is a low mass loss rate object with low optical depths in the lowest rotational transitions. In fact, some of the low lying transitions are inverted over parts of the CSE, i.e., maser action is taking place. In particular, the $J=1\rightarrow 0$ is inverted over the entire CSE producing a line profile that is clearly double peaked, i.e., this is due to maser action and not due to resolution effects. The observations of this transition are complicated by possible contamination by interstellar lines, and the signal-to-noise ratio is not particularly good, erasing any possible signs of maser action. As expected the radiation emitted by the central star plays an important role in the excitation. The transitions exhibiting population inversion are particularly sensitive (both the intensity and line profile) to the physical conditions prevailing in the CSE. In this case where radiative excitation is important the model becomes sensitive to the choice of inner radius, r_i , as well as turbulent velocity, v_t . Here, also the size of the envelope is important when determining the mass loss rate, i.e., the emission is photodissociation limited (at least for the lowest transitions). Generally, the line intensities scale roughly linearly with \dot{M} .

R For presents an intermediate case between LP And and W Ori. It is also a typical sample star in the sense that the majority of the stars have envelope parameters that resemble those of R For. From Table 5 and Fig. 7 we see that R For shares properties of both the low and the high mass loss rate star. An intermediate mass loss rate model is generally more sensitive to the temperature structure than the radiation field, thus resembling the high mass loss rate objects. However, as in the low mass loss rate regime the line intensities scale roughly linearly with \dot{M} . We also note that the derived line intensities, especially the $J=1\rightarrow 0$ transition, start to become sensitive to the outer radius of the CO envelope. The exact mass loss rate where the transition from photodissociation- to excitation-limited emission occurs is hard to pinpoint, since it depends on the envelope characteristics. We have made tests which show that for typical

envelope parameters the transition lies at $\sim 5 \times 10^{-7} M_{\odot} \text{yr}^{-1}$ for the $J=1\rightarrow 0$ transition. Higher J -lines sample hotter and denser gas, located closer to the star, and are therefore less sensitive to the choice of the envelope size.

In summary, we believe that within the adopted circumstellar model, the estimated mass loss rates are accurate to about $\pm 50\%$ (neglecting errors introduced by the uncertain CO abundance and the distance estimates) when good observational constraints are available, but one should keep in mind that the causes of the uncertainty varies with the mass loss rate.

Another rough way to estimate the errors involved is to compare with the results obtained from other self-consistent models. When comparing our mass loss rate estimate for CW Leo to those obtained from detailed radiative transfer models (Kastner 1992; Crosas & Menten 1997; Groenewegen et al. 1998a; Skinner et al. 1999) we find a very good agreement, within 20 %, when adjustments for differences in f_0 and distance have been made. Kastner (1992) also modelled the high mass loss rate object RW LMi (a.k.a. CIT 6) and obtained a mass loss rate in excellent agreement with our estimate (when corrected for the difference in distance). Recently, Hiriart & Kwan (2000) presented a method to combine a circumstellar dust model with a CO model, keeping physical quantities consistent between the models. They present mass loss rate estimates for 17 of our sample stars. Based upon their Eq. 17 and Table 6 we derive hydrogen mass loss rates for these stars that are, on the average, 1.3 times larger than those derived from our radiative transfer analysis (for an individual star, however, the discrepancy can be as large as a factor of 3).

We also compare our derived mass loss rates with those obtained by Olofsson et al. (1993a) using a formula based on the work by Knapp & Morris (1985),

$$\dot{M}_{\text{KM}} = 5.7 \times 10^{-20} \frac{T_{\text{mb}} v_{\text{e}}^2 D^2 \theta_{\text{mb}}^2}{s(J) f_0^{0.85}} \text{ M}_{\odot} \text{yr}^{-1}, \quad (14)$$

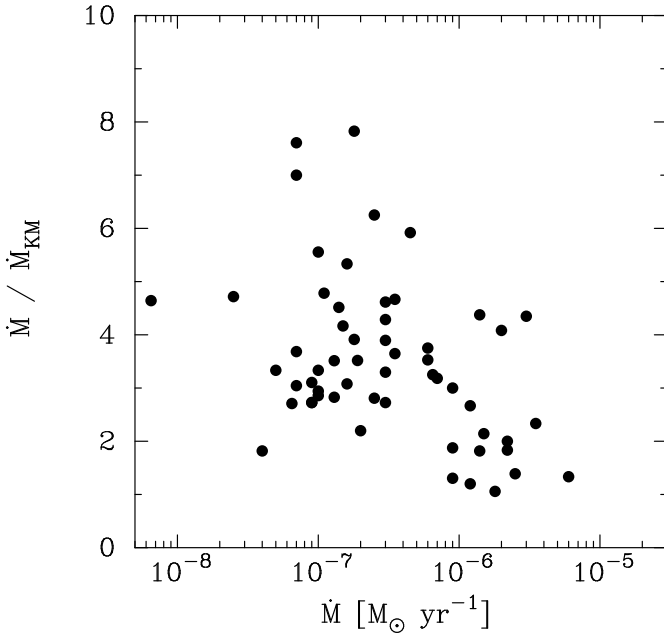


Fig. 8. The ratio of the estimated mass loss rates from our radiative transfer analysis (\dot{M}) to those estimated from an analytical formula (\dot{M}_{KM}) (see text for details).

which relates the mass loss rate \dot{M}_{KM} to easily determined observables (T_{mb} is given in Kelvins, v_e in km s^{-1} , D in pc, and θ_{mb} in arcseconds). In Eq. 14 $s(J)$ is a factor that depends on the transition (J) used. For $J=1 \rightarrow 0$ $s(J)=1$ and for $J=2 \rightarrow 1$ $s(J)=0.5$ (see the discussion in Olofsson et al. 1993a). When estimating the mass loss rates from Eq. 14 we have used the observed $J=1 \rightarrow 0$ and $J=2 \rightarrow 1$ line emission, and averaged the results. This mass loss rate was compared to that obtained from the radiative transfer analysis, Fig. 8. It is found that Eq. 14 significantly underestimates the mass loss rates when compared to those obtained from the radiative transfer analysis by, on the average, a factor of about four. However, considering the simplicity of Eq. 14 the agreement is remarkably good. There is also a trend that the discrepancy increases with lower mass loss rate (indeed Olofsson et al. suspected that their simple approach led to a systematic underestimate of the mass loss rate that became worse the lower the mass loss rate). In this context it should be noted that Eq. 14 was derived assuming a fixed CO envelope size of $3 \times 10^{17} \text{ cm}$, which is appropriate for high mass loss rate objects. In the high mass loss rate regime the line intensities are not very sensitive to the exact envelope size since the emission is excitation limited. This is, however, generally not the case for the optically bright carbon stars in our sample, where the line intensities are sensitive to the size of the CO envelope set by photodissociation. A correction for the envelope size [see Neri et al. (1998) and references therein] would decrease the discrepancy seen in Fig. 8 for the stars losing mass at lower rates. Taken at face values the discrepancies between the mass loss rates derived here and those derived by Olofsson et al. (1993a) are smaller, but this is due to the fact that on the average Olofsson et al. used larger distances. This also means

that the trend in the dust-to-gas mass ratio, decreasing with the mass loss rate, that Olofsson et al. reported was due to underestimating gas mass loss rates [see also Hiriart & Kwan (2000)]. Indeed, in Sec. 4.2 we find the opposite behaviour, i.e., indications of a dust-to-gas mass ratio that increases with the mass loss rate.

4.4. The CO envelope sizes

The size of the CO envelope is an important parameter, and the derived mass loss rate will depend on it to an extent that depends on the mass loss rate (see discussion in Sec. 4.3). Neri et al. (1998) presented IRAM PdB interferometer (PDBI) CO($J=1 \rightarrow 0$) maps of varying quality for 9 of our sample stars. From their CLEANed brightness maps we have obtained the averaged radial brightness distributions. In addition, we have obtained two single-dish CO($J=1 \rightarrow 0$) maps using the OSO 20 m telescope. In Fig. 9 we compare the observed radial brightness distributions to those calculated from our model, which uses the Mamon et al. (1988) results to estimate the CO envelope size, for the parameters presented in Tab. 3. We find that the estimated CO envelope sizes are generally consistent with the observations. In four cases (V384 Per, RW LMi, T Dra, and S Cep) the calculated radial brightness distributions fail to reproduce the observations. At least in the case of V384 Per and RW LMi this appears to be due to deviations from a simple r^{-2} density law, in the sense that two distinct components are clearly visible in the brightness maps.

We are not able to distinguish between the different CO envelope sizes obtained by Mamon et al. (1988) and Doty & Leung (1998) for the high mass loss rate object CW Leo. This is simply because the emission in this case is excitation limited with the external cool and tenuous parts producing very little emission.

4.5. The kinetic temperature structure

As was demonstrated in Sec. 4.3 the derived mass loss rate can be very sensitive to the kinetic temperature structure of the gas. Adiabatic cooling alone results in $T(r) \propto r^\delta$, where $\delta = -4/3$ (assuming $\gamma = 5/3$), but from Figs. 4–6 it is evident that other cooling processes as well as heating mechanisms are important. If CO line radiation is the dominant cooling mechanism and $n > n_{crit}$ one would expect $T(r) \propto r^{-1}$ with a somewhat shallower decline if $n < n_{crit}$ (see Doty & Leung 1997).

Generally, it is not possible to assign a simple power law to the radial behaviour of the temperature throughout the entire CSE. However, in the case of LP And we find $\delta \sim -0.9$ for $r \lesssim 5 \times 10^{16} \text{ cm}$. Further out in the cool, tenuous, outer layers of this CSE, heating due to the photoelectric effect is important and raises the temperature. For R For and W Ori we estimate, over the regions where the observed emissions emanate, i.e., from $\sim 1 \times 10^{15}$ to $\sim 5 \times 10^{16} \text{ cm}$, δ to be ~ -0.7 for both sources. For comparison, Doty & Leung (1997) derive $\delta \sim -1.0$ for the high mass loss rate object CW Leo, while we obtain $\delta \sim -0.9$.

From the fact that $C \propto \dot{M}$ and $H \propto \dot{M}^{0.5}$ one would expect high mass loss rate objects to have significantly cooler envelopes than low mass loss rate objects (e.g., Jura et al. 1988). In our modelling we do not see this trend. The reason being that in addition $H \propto h(L_{\text{ve}})^{3/2}$, where all of the parameters have a mass loss rate dependence in the sense that their values are generally smaller for the low mass loss rate objects.

4.6. ^{13}CO line cooling

Carbon stars generally have $^{12}\text{C}/^{13}\text{C}$ -ratios in the range 30–70 (Lambert et al. 1986; Schöier & Olofsson 2000). This means that for the large majority of all stars in our sample line cooling by ^{13}CO is insignificant, even when optical depth effects are taken into account. However, there exists a small population of carbon stars, the J-type stars, which have $^{12}\text{C}/^{13}\text{C}$ -ratios of ~ 3 . For these stars ^{13}CO line cooling could be important.

To test this we have included ^{13}CO line cooling for one of our sample stars, Y CVn, a known J-type star. We have used the ^{13}CO model as presented in Schöier & Olofsson (2000) to calculate the contribution from this isotopomer to the total amount of cooling, and used this extra cooling term as input to the standard model. We find that, after we have iterated between the ^{12}CO and ^{13}CO models a few times, that ^{13}CO line cooling is somewhat less effective as a coolant than expected, based on the isotope ratio (probably due to slightly different excitation conditions between the two molecules). The effect on the derived line intensities is small; the largest effect is on the $J=3 \rightarrow 2$ line emission which is lowered by $\sim 10\%$. The changes in line intensity may be compensated for by increasing the h -parameter.

Moreover, Ryde et al. (1999) present a model of the high mass loss rate object IRAS+15194-5115 using the radiative transfer code outlined here. The $^{12}\text{C}/^{13}\text{C}$ -ratio for this object was estimated to be 5.5, i.e., it resembles the J-type stars in this respect. It was found that ^{13}CO line cooling in this case was approximately one third of that of ^{12}CO (due to optical depth effects the ^{13}CO line cooling is in a relative sense more important). The decrease in kinetic temperature due to this extra cooling was compensated for by the fact that the h -parameter (heating) had to be somewhat increased to produce the observed line intensities. Consequently, the derived mass loss rate was not affected by introducing the ^{13}CO line cooling.

5. Deviations from the standard model

For some stars, where there are enough observational constraints, it is possible to establish deviations from the standard model.

5.1. Detached CSEs

In our sample there exist a number of stars that exhibit a $60\text{ }\mu\text{m}$ excess, placing them in the regions VIa and VIb in the IRAS colour-colour diagram (see Olofsson et al. 1993a), suggesting that their CSEs are abnormal in some way. Previous CO obser-

vations of five of these $60\text{ }\mu\text{m}$ excess stars (see Table 6) have revealed that their CSEs cannot have been produced by a single smooth expanding wind, but rather suggested a drastic modulation of the mass loss on a time scale as short as a thousand years, which produced detached CSEs (dCSEs; Olofsson et al. 1996b). Presently, these stars are losing matter at a significantly lower rate, forming what is referred to as an attached circumstellar envelope (aCSE).

To be able to put constraints on the mass loss and its variation with time, high spatial resolution observations are needed. Such observations have been carried out using the IRAM PdB interferometer, with an angular resolution of $\sim 1''$, for two of the stars in Table 6, U Cam and TT Cyg. It was found that the dCSE around U Cam is fairly young while that around TT Cyg is significantly older. Both dCSEs show a remarkable overall spherical symmetry, and they are geometrically very thin. The CO line emission towards these two sources, supplemented by a detailed modelling using the radiative transfer code outlined in this paper, were presented in Lindqvist et al. (1999) (U Cam) and Olofsson et al. (1998, 2000) (TT Cyg).

In this paper we have attempted to model the remaining three stars with known detached shells (R Scl, S Sct, and U Ant), based upon the results obtained from the high angular resolution observations described above. The results for both the aCSEs and dCSEs around these stars are presented in Table 6 (where also the results for TT Cyg and U Cam are included). Due to the limited observational constraints available, the dCSEs around S Sct and U Ant were modelled using the same geometrical thickness and kinetic temperature structure as obtained for TT Cyg (Olofsson et al. 2000). For R Scl we used the same geometrical thickness as adopted by Olofsson et al. 1996b and assumed a kinetic temperature decreasing linearly with radius from a value of 50 K at the inner shell radius. The derived intensities from the model generally agree well with those observed (Table 7). However, we note that in the case of R Scl we only get about half of the observed $J=3 \rightarrow 2$ line emission from the model, but here the aCSE could produce a significant amount of the observed emission. We find that the estimated shell masses, M_s , are relatively similar, but there is a trend of increasing shell mass with age (the R Scl shell mass may be overestimated due to the difficulty in separating the aCSE and dCSE emission), which may indicate that gas is being swept up.

The present mass loss rate was modelled for U Ant and S Sct using the standard model. The results are presented in Table 6 and Table 7. For R Scl the emission from the aCSE and dCSE cannot be separated. Again, the predicted line intensities agree, with one exception, well with those observed, considering the uncertainties of the observations. For S Sct the model of the aCSE fails to reproduce the IRAM CO($J=2 \rightarrow 1$) observations, in contrast to the dCSE model where the fit to the observations is excellent. An explanation to this inconsistency could be that there are pointing problems in these observations (the IRAM observations are more sensitive to the pointing due to its smaller beam), which would mainly affect the emission observed from the aCSE. We find that the present mass loss

Table 6. Model results for the sources with known detached shells (see text for details)

Source	Var. type	P [days]	D [pc]	aCSE			dCSE				
				\dot{M} [M_{\odot} yr $^{-1}$]	v_e [km s $^{-1}$]	r_p [cm]	\dot{M}_s [M_{\odot} yr $^{-1}$]	v_s [km s $^{-1}$]	r_s [cm]	Δr_s [cm]	M_s [M_{\odot}]
R Scl ¹	SRb	370	360				4.0×10^{-6}	16.5	7.0×10^{16}	7.0×10^{16}	5.4×10^{-3}
U Cam ²	SRb		500	2.5×10^{-7}	12.0	1.4×10^{16}	9.0×10^{-6}	23.0	5.5×10^{16}	1.1×10^{16}	1.4×10^{-3}
U Ant ¹	Lb		260	3.0×10^{-8}	4.5	1.4×10^{16}	1.5×10^{-5}	19.5	1.6×10^{17}	2.0×10^{16}	4.9×10^{-3}
S Sct ¹	SRb	148	400	3.0×10^{-8}	4.5	1.4×10^{16}	4.0×10^{-5}	17.0	4.0×10^{17}	2.0×10^{16}	1.5×10^{-2}
TT Cyg ³	SRb	118	510	3.0×10^{-8}	4.0	1.5×10^{16}	1.5×10^{-5}	12.5	2.7×10^{17}	1.9×10^{16}	7.2×10^{-3}

Model is presented in: ¹ This paper; ² Lindqvist et al. (1999); ³ Olofsson et al. (2000).

Table 7. CO modelling results, for three sources with known detached shells, compared to observations.

Source	Tel.	Trans.	aCSE		dCSE		Ref.
			I_{obs} [K km s $^{-1}$]	I_{mod} [K km s $^{-1}$]	I_{obs} [K km s $^{-1}$]	I_{mod} [K km s $^{-1}$]	
R Scl ^a	SEST	1–0			26.1	29.6	2
	IRAM	1–0			76.2	79.2	1
	SEST	2–1			47.8	49.8	1
	JCMT	2–1			50.6	54.8	3
	IRAM	2–1			67.7	72.0	1
	SEST	3–2			63.7	28.0	2
	JCMT	3–2			62.9	30.5	3
U Ant	SEST	1–0		0.6	10.0	13.4	2
	SEST	2–1	3.2	2.8	7.6	7.3	2
	JCMT	2–1	3.6	3.3	7.7	7.2	3
	SEST	3–2	3.6	4.0	5.0	3.0	2
S Sct	SEST	1–0		0.3	5.3	5.6	1
	IRAM	1–0	2.5:	1.3	5.3	5.4	1
	SEST	2–1	1.1	1.3	2.7	2.9	2
	JCMT	2–1	0.9	1.3	2.4	3.0	3
	IRAM	2–1	1.8:	5.4	2.8	2.8	1
	SEST	3–2	2.1	1.7	1.0	0.9	2
	JCMT	3–2	2.4	2.2	1.0	0.9	3

^a For this source it is not possible to separate the contributions from an aCSE and a dCSE; 1. Olofsson et al. (1993a); 2. Olofsson et al. (1996); 3. JCMT public archive

rates of the stars with the oldest shells are low, and that the present mass loss rate of U Cam (which has a much younger dCSE) is significantly higher.

The central stars are semi-regular (SR) or irregular variables (Lb), and they have low present mass loss rates. They appear to have been subject to drastic modulations of their mass loss rates over relatively short periods of time (a few thousand years). We estimate that the CO dCSE emission is observable for $\sim 10^4$ years (Bergman et al. 1993). If this mass ejection is a repeatable phenomenon, and all our sample stars go through this phase, we estimate that the time scale between mass ejections is about 10^5 years. Therefore, the mass ejections may possibly be linked with the helium-shell flashes (the process that leads to nuclear-processed matter being transported to the surface of the star) predicted to occur regularly in AGB stars with time intervals of the order of 10^5 years for the relevant masses (e.g., Blöcker 1995). We note that *all* carbon stars that have been found to have clearly detached gas shells are members of

our sample, and that no M-type star with a detached CO shell has been detected.

5.2. V Hya and TX Psc

The successful modelling of the vast majority of our sample stars, assuming a spherically symmetric CSE, suggests that axi- or non-symmetric mass loss is not a common phenomenon among these optically bright carbon stars. However, in the case of V Hya and TX Psc, stars with complex radio line profiles, the possibility of bipolar outflows has been considered (Heske et al. 1989; Kahane et al. 1996). Due to the complexity of these outflows, no radiative transfer analysis was attempted here.

Kahane et al. (1996) suggest that V Hya, in addition to the high velocity bipolar outflow, has a slowly expanding spherical component. Using a 2D radiative transfer code, based upon the Sobolev approximation, they derive a total mass loss rate of $\sim 1.5 \times 10^{-6} M_{\odot} \text{yr}^{-1}$ for this object. The authors further sug-

gest that V Hya is a transition object, between carbon stars and PNe, having just developed a highly axi-symmetric mass loss. The slowly expanding spherical component is then interpreted as the fossil CSE created during the AGB stage. Knapp et al. (1999), however, argue, based upon the spectral type, period, colours, and lack of ionizing radiation, that V Hya is still on the AGB. Moreover, they estimate the total mass loss rate of this object to be $\sim 4 \times 10^{-5} M_{\odot} \text{yr}^{-1}$. This, in addition to the small dynamical age of the envelope, suggests that V Hya has entered its "superwind" phase.

The observed line profiles of the CO line emission towards TX Psc are somewhat peculiar (Heske et al. 1989; Olofsson et al. 1993a). As a consequence, the expansion velocity derived from the observed radio line profiles range from 7.5 to 12.2 km s^{-1} (see Table 2 and Olofsson et al. 1993a) depending on the transition and the telescope used. Heske et al. (1989), mapped the circumstellar CO line emission around this object, and interpreted the observed asymmetries as being produced either by a bipolar outflow or a highly clumped wind. No detailed modelling exist for the CSE around TX Psc, and its evolutionary status remains uncertain. It might be in a state similar to that of V Hya.

5.3. DR Ser

DR Ser has the highest $60 \mu\text{m}$ excess of all the sample stars, which places it in the IRAS two-colour diagram among objects having detached envelopes (see Table 6). Indeed, Kerschbaum (1999) suggests that this might be a detached shell source based upon his modelling of the SED of this object. However, the CO single dish observations reveal no signs of double-peaked profiles (confusion with interstellar lines complicates the interpretation), which are indicative of a detached CO shell. Moreover, DR Ser has a relatively low $^{12}\text{C}/^{13}\text{C}$ -ratio of 6 (Abia & Isern 1997). Thus, it resembles the J-type stars.

Attempting to model this source with a standard model of its CSE fails to explain both the observed $J=1 \rightarrow 0$ and $J=2 \rightarrow 1$ line intensities in that they come out too weak, by more than a factor of two. This is due to the extremely cold envelope, resulting from the adopted h -parameter of 0.2 (due to the luminosity being lower than $6000 L_{\odot}$), in combination with a relatively high mass loss rate $\sim 2 \times 10^{-6} M_{\odot} \text{yr}^{-1}$ required to maximize the line intensities. Further increasing the mass loss rate will make the envelope even cooler due to the increase in CO line cooling. If one instead assigns an h -parameter of ~ 1 it is possible to obtain a reasonable fit to the data using a mass loss rate of $\sim 5 \times 10^{-6} M_{\odot} \text{yr}^{-1}$. This estimate must be regarded as highly uncertain.

6. Discussion

6.1. The mass loss rate distribution

Fig. 10 shows the distribution of the mass loss rates obtained from the radiative transfer model for all sources (also shown is the distribution for the stars within 500 pc of the Sun), as well

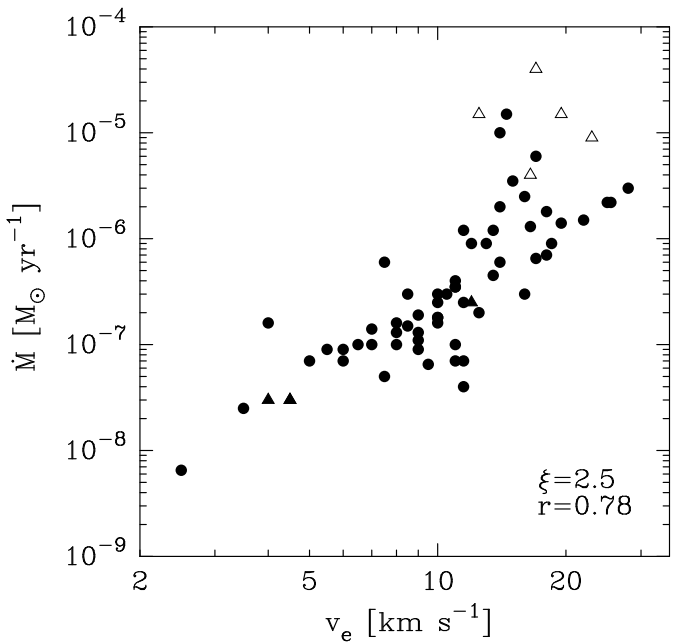


Fig. 11. The derived mass loss rate plotted against the gas expansion velocity of the CSE. Sources with known detached shells are indicated with triangles (open triangles represent dCSEs, while filled ones represent aCSEs). \dot{M} scales as v_e^{ξ} , with $\xi=2.5$. Also shown is the correlation coefficient r .

as divided into variability groups (note that objects with known detached shells have not been included in this analysis). Since the statistics of the SRa stars are poor we have chosen to group them together with the SRb stars. The mass loss rate distribution for all stars is sharply peaked around the median mass loss rate of $2.8 \times 10^{-7} M_{\odot} \text{yr}^{-1}$ (the median mass loss rate for the stars within 500 pc of the Sun is $1.6 \times 10^{-7} M_{\odot} \text{yr}^{-1}$). It is interesting to note that this is roughly the rate at which the core mass is expected to grow due to nuclear burning (Schönberner 1983). Mira variables generally have larger mass loss rates than other variability types, while irregular variables and semiregulars appear to have very similar mass loss rate characteristics.

Based on the mass loss rate distribution for the sample of stars within 500 pc, which we believe to be close to complete and for which we have detected all sources, we are able to draw some general conclusions. The sharp decline at mass loss rates below $\sim 5 \times 10^{-8} M_{\odot} \text{yr}^{-1}$ is very likely real. Netzer & Elitzur (1993) estimate that a mass loss rate in excess of $\sim 10^{-7} M_{\odot} \text{yr}^{-1}$ is required to get a dust-driven wind. The exact limit is, however, sensitive to the adopted stellar and dust parameters. The drastically decreasing number of high mass loss rate objects is also real, although our selection criterion bias against these objects, and can be explained by the fact that carbon stars of the type discussed here, i.e., mainly low mass ones (Claussen et al. 1987), only for a limited time, or possibly never, reach high mass loss rates.

6.2. Mass loss and envelope kinematics

The v_e -distribution for this sample of stars has already been shown and discussed by Olofsson et al. (1993a). However, a new comparison between the mass loss characteristics \dot{M} and v_e is warranted considering the more reliable mass loss rates obtained in this paper, Fig. 11. We find a clear trend that v_e increases with \dot{M} , $v_e \propto \dot{M}^{0.40}$ (with a correlation coefficient of 0.78). In comparison, Olofsson et al. (1993a) derived $v_e \propto \dot{M}^{0.53}$, but their mass loss rates were calibrated using Eq. 14, which includes a v_e^2 -dependence. The correlation is much tighter than that obtained by Olofsson et al. (1993a), which is reassuring. Thus, the mass loss mechanism operates such that mass loss rate and expansion velocity increase together. However, the scatter appears larger than the uncertainties in the estimates, and so the mechanism also produces widely different mass loss rates for a given expansion velocity. At high mass loss rates the scatter is larger with a possible division into objects with high mass loss rates but only moderately high velocities, and objects with moderately high mass loss rates but high velocities. We note also that for the detached shell sources the mass loss rates and expansion velocities for the two mass loss epochs follow the general trend.

Habing et al. (1994) studied the momentum transfer from the photons, via the dust, to the gas in the CSEs of AGB stars. They found that for mass loss rates close to the minimum mass loss rate for a dust-driven wind, $\sim 3 \times 10^{-8} M_\odot \text{ yr}^{-1}$, v_e increases linearly with \dot{M} , while for mass loss rates above $\sim 10^{-6} M_\odot \text{ yr}^{-1}$ the dependence weakens considerably. At $10^{-5} M_\odot \text{ yr}^{-1}$ they found $v_e \propto \dot{M}^{0.04}$. Habing et al. attribute the increase in v_e with mass loss rate (for low mass loss rates) to a higher efficiency in the coupling between gas and dust. This can explain the observed behaviour in Fig. 11 for mass loss rates below about $10^{-6} M_\odot \text{ yr}^{-1}$, but for the higher mass loss rates it appears that a dependence of v_e (and \dot{M}) on luminosity gives the most reasonable explanation, see Sect. 6.3.

6.3. Dependence on stellar properties

In Fig. 12 we plot the circumstellar characteristics, \dot{M} and v_e , against the stellar characteristics luminosity (L), period (P), effective temperature (T_{eff}), and the photospheric C/O-ratio. The effective temperatures and C/O-ratios used in this analysis are those presented in Olofsson et al. (1993b). We have looked for dependences assuming that the ordinate scales as the abscissa to the power of ξ , and a normal correlation coefficient r was calculated as an estimate of the quality of the fit, see Fig. 12. The uncertainties in the estimated quantities are of the order: $\pm 50\%$ (\dot{M}), $\pm 2 \text{ km s}^{-1}$ (v_e), $\pm 10\%$ (P ; but some periods may be poorly determined), a factor of 2 (L), and $\pm 200 \text{ K}$ (T_{eff}).

Clearly, both the mass loss rate and the expansion velocity increase with the pulsation period of the star. There is a weaker trend with the luminosity of the star. The latter dependence is not completely independent of the former, since some of the luminosities are estimated from a $P - L$ relation. The existence of a $P - L$ relation is usually attributed to a distribution in mass

(Jones et al. 1994), i.e., the higher the mass the longer the period and the higher the luminosity. When looked at in detail, at least the apparent mass loss rate dependence on period may be attributed to a change from semiregular pulsation at short periods to regular pulsations at longer periods. We may therefore infer that for the mass loss rate it is not clear whether it is the regularity of the pulsation or the luminosity that causes the increase with period. For the expansion velocity the increase with period may be a combined effect of increasing mass loss rate with period (for low mass loss rates) and an increase in luminosity for the longer periods, e.g., Habing et al. (1994) derive $v_e \propto L^{0.35}$ in their dust-driven wind model. In addition, there is evidence of a weak trend in the sense that higher mass loss rate objects have lower effective temperatures. These correlations are all consistent with a dust-driven wind, where the pulsation may play an important role. There appears to be no correlation between the mass loss rate and the C/O-ratio, which is surprising considering that the dust-to-gas mass ratio in a C-rich CSE should be sensitively dependent on this.

The present mass loss rates for the detached shell sources are typical for their periods but somewhat low for their luminosities. However, during the formation of the dCSEs the mass loss rate must have been atypically high for the present periods and luminosities. We also find that the expansion velocities of the dCSEs lie at the very high end of expansion velocities found for other stars with the same luminosity, indicating that these stars had higher luminosities during the shell ejection.

Two other stars, SZ Car and WZ Cas, stand out in these plots. The properties of SZ Car resembles the stars with known dCSEs, but the CO line profiles give no indication of a detached shell. WZ Cas has by far the lowest estimated mass loss rate in the sample, as well as the lowest C/O-ratio, 1.01, which classifies it as an SC-star. It is also a Li-rich J-star (Abia & Isern 1997).

6.4. Enrichment of the ISM

Carbon stars on the AGB are important in returning processed gas to the interstellar medium (ISM). The total mass loss rate of carbon stars in the Galaxy is obtained from

$$\dot{M}_{\text{Gal}} = \int_0^\infty 2\pi R \Sigma \langle \dot{M} \rangle dR \quad (15)$$

where Σ is the surface density of carbon stars, $\langle \dot{M} \rangle$ is the mean mass loss rate of the carbon stars. According to Guglielmo et al. (1998) the infrared carbon stars have a roughly constant surface density out to the galactocentric distance of the Sun, after which it follows an exponential decline with a scale length of $\sim 2.5 \text{ kpc}$. We approximate this by assuming a constant value, Σ_0 (the surface density in the solar neighborhood), to 10 kpc and zero beyond this galactocentric distance.

Based on the complete sample, i.e., stars within 500 pc from the Sun, we estimate $\Sigma_0 \langle \dot{M} \rangle$ to be $\sim 1.7 \times 10^{-10} M_\odot \text{ yr}^{-1} \text{ pc}^{-2}$, where we have included also helium. This estimate is very sensitive to the number of high mass loss rate objects found within 500 pc , e.g., the high

mass loss rate object CW Leo contributes almost half of our estimate of the total mass returned to the ISM. Our estimate of the rate at which matter is returned to the ISM by carbon stars is consistent with previous estimates (considering the large uncertainties), e.g., Knapp & Morris (1985) and Jura & Kleinmann (1989) derive values of $\sim 2 \times 10^{-10} M_{\odot} \text{ yr}^{-1} \text{ pc}^{-2}$ and $\sim 1.5 \times 10^{-10} M_{\odot} \text{ yr}^{-1} \text{ pc}^{-2}$, respectively. Using Eq. 15 the annual return of matter to the ISM in the Galaxy is estimated to be $\sim 0.05 M_{\odot}$ for the carbon stars considered here. It is quite possible that a larger mass return from carbon stars is obtained during their final evolution on the AGB, a so called superwind phase, as is indicated by the estimated values for infrared carbon stars, $\sim 0.5 M_{\odot} \text{ yr}^{-1}$ (Epchtein et al. 1990; Guglielmo et al. 1993), and PNe, $\sim 0.3 M_{\odot} \text{ yr}^{-1}$ (Gustafsson et al. 1999). This confirms the importance of carbon stars for the cosmic gas cycle in galaxies. By comparison, high mass stars are estimated to contribute about $0.04 M_{\odot} \text{ yr}^{-1}$ (Gustafsson et al. 1999).

We estimate the contribution from carbon stars to the carbon enrichment of the ISM to be $\sim 0.5 \times 10^{-4} M_{\odot} \text{ yr}^{-1}$ during the AGB stage (if the subsequent superwind phase is included this value may increase to $\sim 5 \times 10^{-4} M_{\odot} \text{ yr}^{-1}$). This corroborates the conclusions by Gustafsson et al. (1999) that ‘normal’ carbon stars are not important for the total carbon budget of the Galaxy. According to these authors the main contributors should instead be high mass stars in the Wolf-Rayet stage, annually supplying the Galaxy with $\sim 0.01 M_{\odot}$ of carbon. This is roughly what is required to produce the $\sim 10^{-3} \times 10^{11} M_{\odot}$ of carbon present in the Milky Way over a period of 10^{10} years.

7. Conclusions

We have developed a detailed radiative transfer code to model circumstellar molecular line emission. The code also solves for the energy balance equation of the gas. It is found that the mass loss rate determination for low mass loss rate objects depends crucially on a number of assumptions in the CSE model, except on the dust properties, since the CO molecules are radiatively excited. On the other hand, the mass loss rate estimate for a high mass loss rate object depends essentially only on the temperature structure, and hence the uncertain dust parameters. In addition, for such an object the CO emission saturates, and becomes less useful as a mass loss rate measure. We also find that different lines respond differently to changes in the various parameters. Therefore, a reliable mass loss rate determination requires, in addition to a detailed radiative transfer analysis, good observational constraints in the form of multi-transition observations and radial brightness distributions.

This model has been applied to CO radio line observations of a large sample of optically bright N-type and J-type carbon stars on the AGB (69 objects). The sample is reasonably complete out to about 1 kpc, and all stars (41) within ~ 500 pc of the Sun have been detected in circumstellar CO line emission. The derived mass loss rates span almost four orders of magnitude, $\sim 5 \times 10^{-9} M_{\odot} \text{ yr}^{-1}$ to $\sim 2 \times 10^{-5} M_{\odot} \text{ yr}^{-1}$, over which the physical conditions of the CSEs vary considerably. The fact

that the model can be successfully applied over such a wide range of environments gives us confidence in the results, even though we are aware of the fact that some assumptions are poorly constrained. The large majority of the stars have mass loss rates in a narrow range centered at $\sim 3 \times 10^{-7} M_{\odot} \text{ yr}^{-1}$, and it appears that very few AGB carbon stars ($\lesssim 5\%$) lose matter at a rate less than $\sim 5 \times 10^{-8} M_{\odot} \text{ yr}^{-1}$.

We find that the mass loss rate and the gas expansion velocity are relatively well correlated, but the scatter is large enough that we may conclude that the mass loss mechanism is able to produce a wide range of mass loss rates for a given expansion velocity. The mass loss rate is also well correlated with the pulsational period of the star, correlated with the stellar luminosity, and there is a weak trend with the stellar effective temperature, in the sense that the cooler stars tend to have higher mass loss rates. Also the gas expansion velocity is positively correlated with the period and the luminosity. We conclude that the mass loss rate increases with increased regular pulsation and/or luminosity, and that the expansion velocity increases with mass loss rate (for low mass loss rates) and luminosity. The observed trends are all supporting the common consensus that these winds are driven by radiation pressure on dust grains, and that pulsation may play an important role. Somewhat surprising there appears to be no dependence on the stellar C/O-ratio.

Our standard CSE model, assuming a single smooth expanding wind produced by a continuous mass loss, fails to reproduce the observational data for about 10% of the sample stars. Most notable among these are five stars with detached CSEs, presumably formed during a period of highly increased mass loss, and low present mass loss rates. We have found indications that the present mass loss rate is significantly higher for the star with the youngest dCSE, and that the shell mass may increase with shell age. Since our sample is reasonably complete, we can estimate that the time scale between mass ejections is about 10^5 years, if it is a repeatable phenomenon. An association with He-shell flashes is favoured. These objects have been the targets of a number of extensive, observational and theoretical studies.

For some of our sample stars there exist enough observational constraints to determine a combined dust parameter from the kinetic temperature structure. This result can be interpreted as a dust-to-gas mass ratio which increases with mass loss rate, but changes in the dust properties may also play a role. We also find that this means that the gas kinetic temperature in a carbon star CSE depends only weakly on the mass loss rate.

The size of the CO envelope is an important parameter in the mass loss rate determination, at least for the low mass loss rate objects. We have used published radial CO($J=1 \rightarrow 0$) brightness distributions, in combination with the radiative transfer code, to show that the CO photodissociation calculation by Mamon et al. (1988) gives reasonably accurate results. In a few cases the observed radial brightness distributions are clearly different than the model results, suggesting deviations from a simple r^{-2} density law, and hence time-variable mass loss.

We estimate that carbon stars, of the type studied here, return on the order of $0.05 M_{\odot} \text{ yr}^{-1}$ of gas to the ISM making them marginally important for the gas cycle in galaxies. More extreme carbon stars may contribute an order of magnitude more. However, they are probably not important as regards the origin of carbon.

Acknowledgements. We are grateful to Dr. F. Kerschbaum for generously providing estimates of some of the input parameters to the CO modelling, to Dr. R. Liseau for useful comments, and to an anonymous referee for constructive criticism which lead to an improved paper. Financial support from the Swedish Natural Science Research Council (NFR) is gratefully acknowledged.

References

Abia C., Isern J., 1997, MNRAS 289, L11

Bergman P., Carlström U., Olofsson H., 1993, A&A 268, 685

Bernes C., 1979, A&A 73, 67

Blöcker T., 1995, A&A 297, 727

Busso M., Gallino R., Wasserburg G. J., 1999, ARA&A 37, 239

Cernicharo J., Barlow M. J., Gonzalez-Alfonso E., et al., 1996, A&A 315, L201

Chandra S., Maheshwari V., Sharma A., 1996, A&AS 117, 557

Claussen M. J., Kleinmann S. G., Joyce R. R., Jura M., 1987, ApJS 65, 385

Crosas M., Menten K. M., 1997, ApJ 483, 913

Doty S. D., Leung C. M., 1997, MNRAS 286, 1003

Doty S. D., Leung C. M., 1998, ApJ 502, 898

Epcstein N., Le Bertre T., Lepine J. R. D., 1990, A&A 227, 82

Flower D. R., Launay J. M., 1985, MNRAS 214, 271

Gilman R. C., 1972, ApJ 178, 423

Glassgold A. E., Huggins P. J., 1983, MNRAS 203, 517

Goldreich P., Scoville N., 1976, ApJ 205, 144

Groenewegen M. A. T., 1994, A&A 290, 531

Groenewegen M. A. T., van Der Veen W. E. C. J., Matthews H. E., 1998a, A&A 338, 491

Groenewegen M. A. T., Whitelock P. A., 1996, MNRAS 281, 1347

Groenewegen M. A. T., Whitelock P. A., Smith C. H., Kerschbaum F., 1998b, MNRAS 293, 18

Guglielmo F., Epcstein N., Le Bertre T., et al., 1993, A&AS 99, 31

Guglielmo F., Le Bertre T., Epcstein N., 1998, A&A 334, 609

Gustafsson B., Karlsson T., Olsson E., et al., 1999, A&A 342, 426

Habing H. J., Tignon J., Tielens A. G. G. M., 1994, A&A 286, 523

Heske A., Te Lintel Hekkert P., Maloney P. R., 1989, A&A 218, L5

Hiriart D., Kwan J., 2000, ApJ 532, 1006

Höfner S., 1999, in in Asymptotic Giant Branch Stars, IAU Symp. No., Vol. 191, p. 159

Huggins P. J., Olofsson H., Johansson L. E. B., 1988, ApJ 332, 1009

Jones T. J., McGregor P. J., Gehrz R. D., Lawrence G. F., 1994, AJ 107, 1111

Jura M., Kahane C., Omont A., 1988, A&A 201, 80

Jura M., Kleinmann S. G., 1989, ApJ 341, 359

Kahane C., Audino P., Barnbaum C., Morris M., 1996, A&A 314, 871

Kastner J. H., 1992, ApJ 401, 337

Kerschbaum F., 1999, A&A 351, 627

Knapp G. R., Dobrovolsky S. I., Ivezić Z., et al., 1999, A&A 351, 97

Knapp G. R., Morris M., 1985, ApJ 292, 640

Kwan J., Hill F., 1977, ApJ 215, 781

Kwan J., Webster Z., 1993, ApJ 419, 674

Kwok S., 1993, ARA&A 31, 63

Lambert D. L., Gustafsson B., Eriksson K., Hinkle K. H., 1986, ApJS 62, 373

Lindqvist M., Olofsson H., Lucas R., et al., 1999, A&A 351, L1

Mamon G. A., Glassgold A. E., Huggins P. J., 1988, ApJ 328, 797

Neri R., Kahane C., Lucas R., Bujarrabal V., Loup C., 1998, A&AS 130, 1

Netzer N., Elitzur M., 1993, ApJ 410, 701

Olofsson H., 1996, Ap&SS 245, 169

Olofsson H., 1997, in Molecules in Astrophysics: Probes & Processes, Vol. 178, p. 457

Olofsson H., Bergman P., Eriksson K., Gustafsson B., 1996, A&A 311, 587

Olofsson H., Bergman P., Lucas R., Eriksson K., Gustafsson B., Bieging J. H., 1998, A&A 330, L1

Olofsson H., Bergman P., Lucas R., Eriksson K., Gustafsson B., Bieging J. H., 2000, A&A 353, 583

Olofsson H., Eriksson K., Gustafsson B., Carlström U., 1993a, ApJS 87, 267

Olofsson H., Eriksson K., Gustafsson B., Carlström U., 1993b, ApJS 87, 305

Ryde N., Schöier F. L., Olofsson H., 1999, A&A 345, 841

Sahai R., 1990, ApJ 362, 652

Schöier F. L., 2000, Ph.D. thesis, Stockholm Observatory

Schöier F. L., Olofsson H., 2000, A&A 359, 586

Schönberg K., 1985, A&A 148, 405

Schönberner D., 1983, ApJ 272, 708

Skinner C. J., Justtanont K., Tielens A. G. G. M., et al., 1999, MNRAS 302, 293

Stanek K. Z., Knapp G. R., Young K., Phillips T. G., 1995, Ap&SS 100, 169

Straniero O., Chieffi A., Limongi M., et al., 1997, ApJ 478, 332

Wallerstein G., Knapp G. R., 1998, ARA&A 36, 369

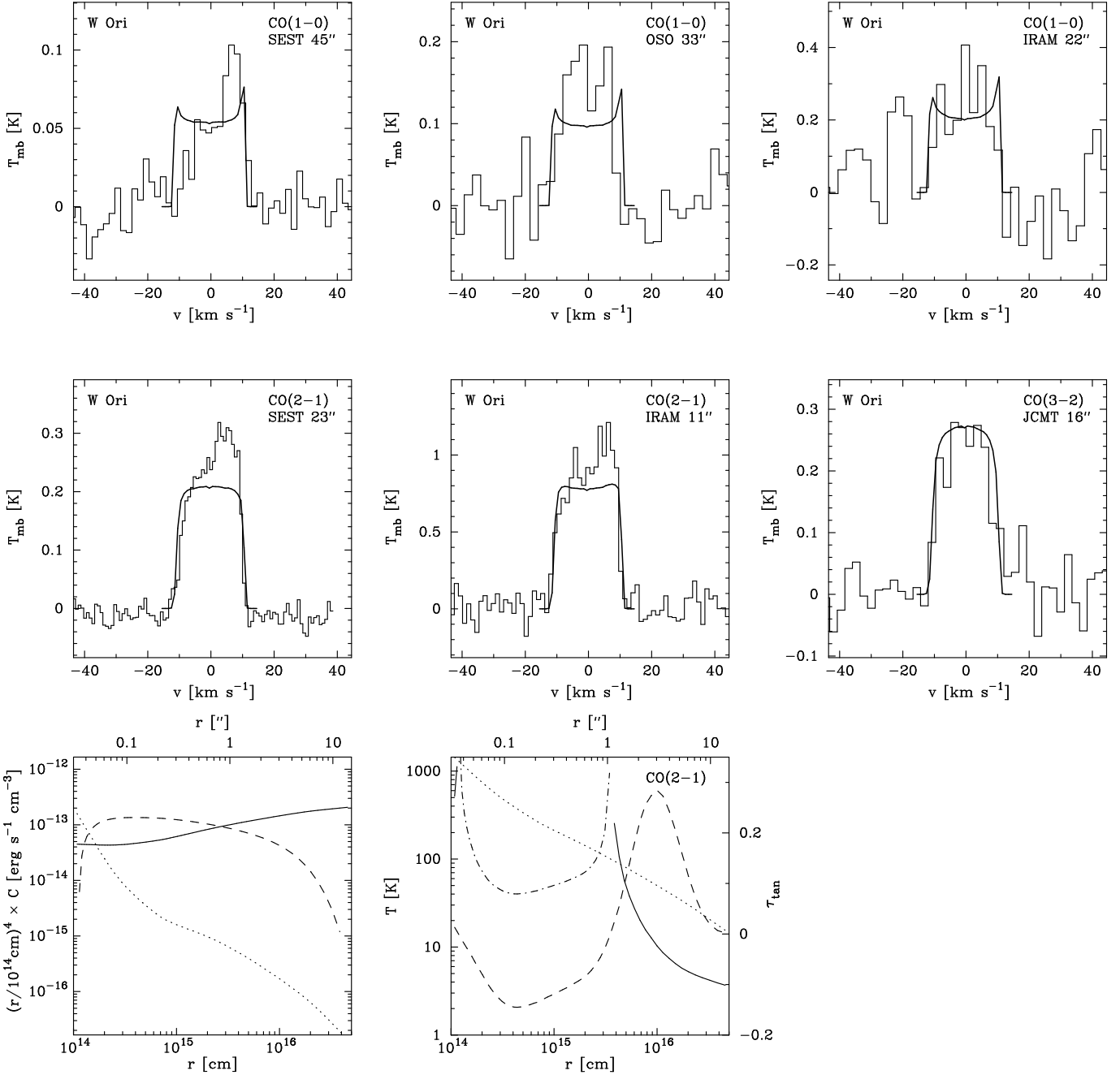


Fig. 6. Multi-transition CO millimetre-wave line emission observed towards the bright carbon star W Ori. The observed spectra (histograms) have been overlayed with the model prediction (full line) using a mass loss rate of $7 \times 10^{-8} M_{\odot} \text{ yr}^{-1}$. The transition, telescope used, and the corresponding beamsize, are indicated for each of the observations. The feature at $\sim 5 \text{ km s}^{-1}$ may be of interstellar origin. The double-peaked profile in the $\text{CO}(J=1 \rightarrow 0)$ model spectra is due to maser action and not due to spatial resolution effects. *Cooling panel*: The full line represents adiabatic cooling; the dotted line gives the H_2 cooling; and the dashed line is CO cooling (see text for details). *Temperature/optical-depth panel*: The dotted line shows the kinetic gas temperature derived from the energy balance equation. The full line gives the excitation temperature of the $\text{CO}(J=2 \rightarrow 1)$ transition, and a dash-dot line indicates a negative excitation temperature, i.e., maser action. The dashed lines give the tangential optical depth, τ_{\tan} , of the $\text{CO}(J=2 \rightarrow 1)$ transition.

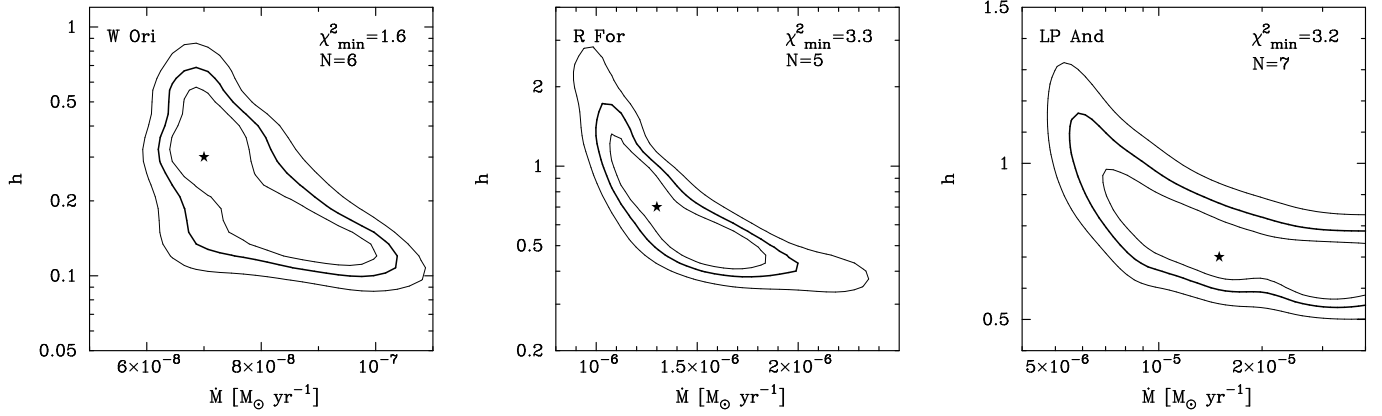


Fig. 7. χ^2 maps showing the sensitivity of the model to the adjustable parameters, i.e., the mass loss rate (\dot{M}) and the h -parameter. Contour levels are drawn at $\chi^2_{\text{min}} + (1.0, 2.3, 4.6)$ with the middle contour (thick line) indicating the 68% confidence level. The best-fit model, as reported in Tab. 3, is indicated by a star and its corresponding χ^2 and the number of observational constraints are also shown.

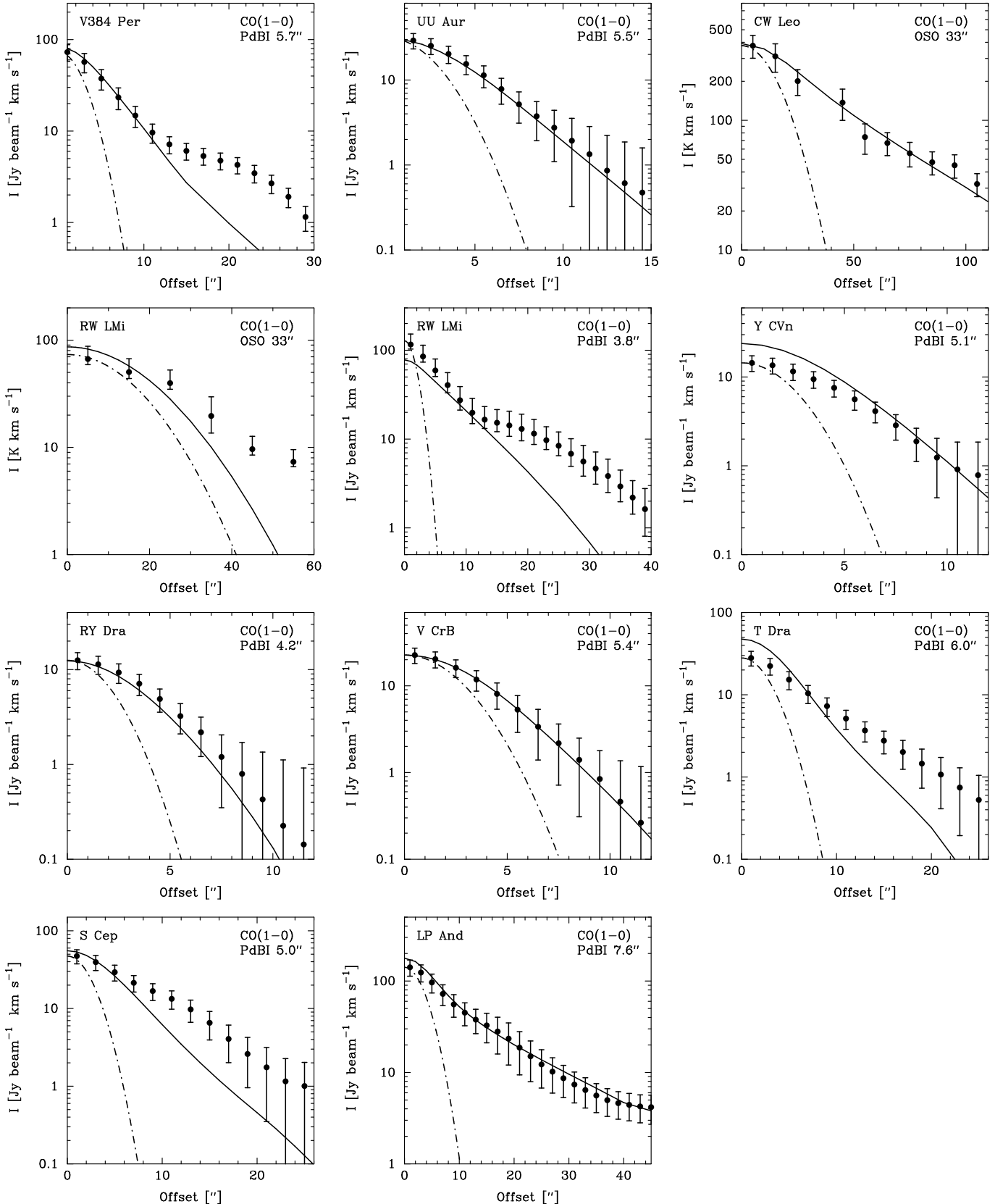


Fig. 9. Observed averaged radial brightness distributions overlayed by the results from the model, using the envelope sizes obtained from the chemical model by Mamon et al. (1988), for the parameters presented in Tab. 3. The circular beam used in the radiative transfer calculation is indicated by the dot-dashed line. Observational errors include both statistical errors and a 20% calibration uncertainty.

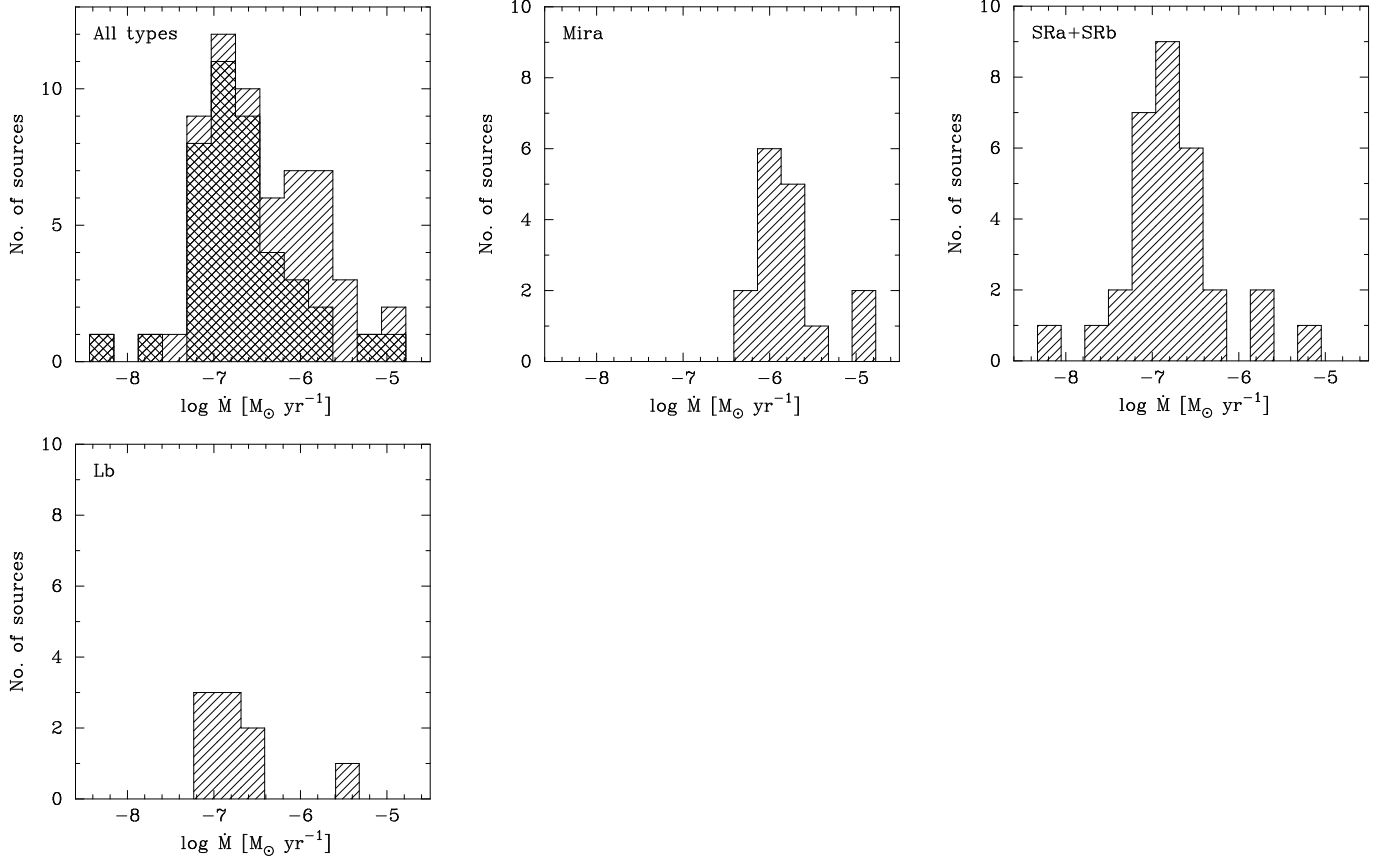


Fig. 10. Histograms showing the distribution of the mass loss rates for the whole sample (upper left panel), as well as subdivided into the different variability types (excluding LP And). Stars with known detached shells have not been included in these plots. In the upper left panel the "cross-hatched" area indicates the mass loss rate distribution for the stars within 500 pc of the Sun, i.e., the complete sample.

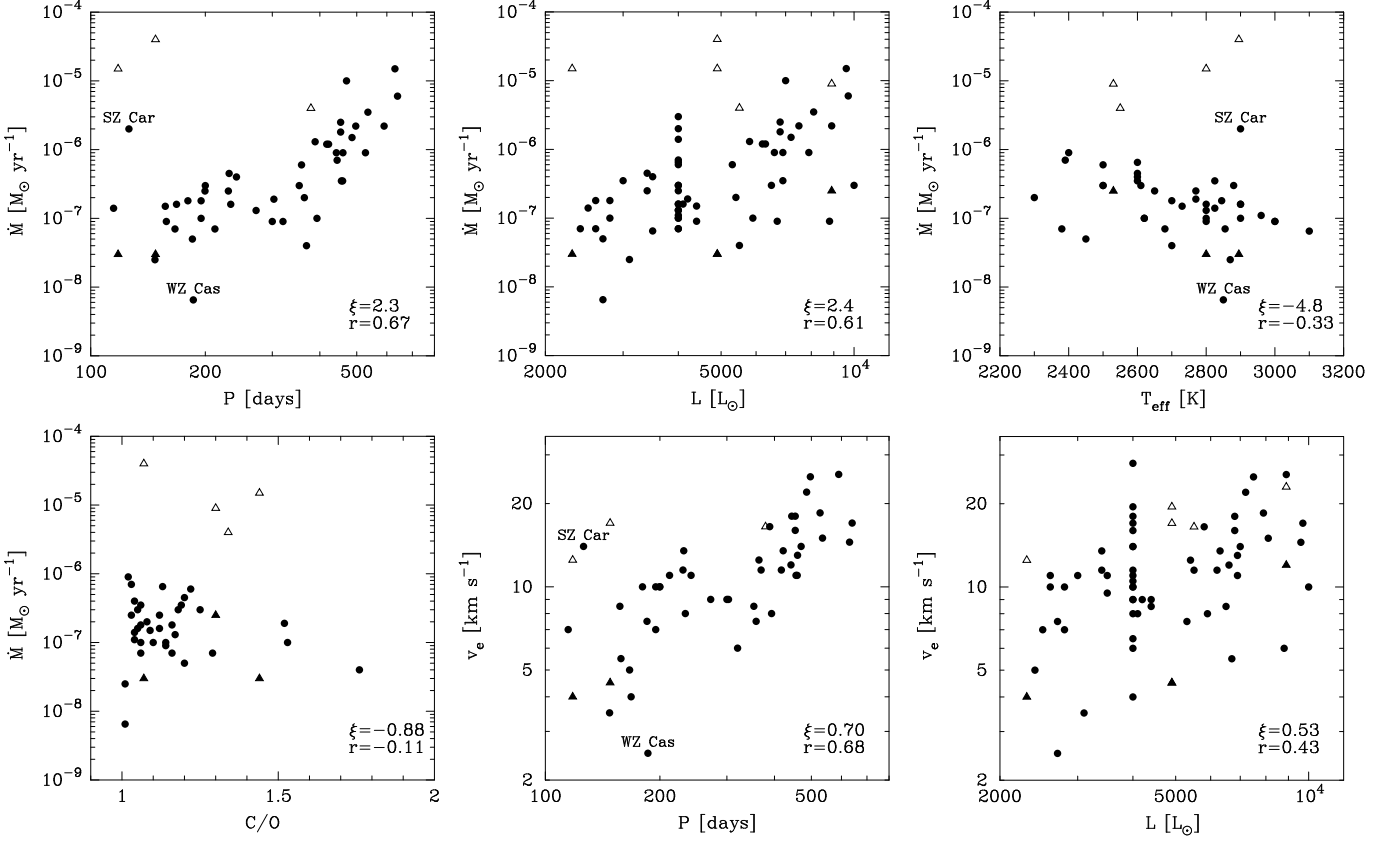


Fig. 12. The derived mass loss rate plotted against the luminosity (L), pulsational period (P), effective temperature (T_{eff}), and the photospheric C/O-ratio of the star. The measured expansion velocity is plotted against the period and the luminosity. Sources with known detached shells are indicated with triangles (open triangles represent dCSEs, while filled ones represent aCSEs). Also shown are the power law index ξ , assuming the ordinate to scale with the abscissa, as well as the correlation coefficient r (the detached shell sources are not included in the fit).